bioRxiv preprint doi: https://doi.org/10.1101/816959; this version posted May 5, 2021. The copyright holder for this preprint (which was not certified by peer review) is the author/funder, who has granted bioRxiv a license to display the preprint in perpetuity. It is made available under aCC-BY 4.0 International license.

A CTP-dependent gating mechanism enables ParB spreading on DNA in *Caulobacter crescentus*

Adam S. B. Jalal[1], Ngat T. Tran[1], Clare. E. M. Stevenson[2], Afroze Chimthanawala[3], Anjana Badrinarayanan[3], David M. Lawson[2], and Tung B. K. Le[1*]

[1]Department of Molecular Microbiology
John Innes Centre, Norwich, NR4 7UH, United Kingdom
[2]Department of Biological Chemistry
John Innes Centre, Norwich, NR4 7UH, United Kingdom
[3]National Centre for Biological Sciences
Tata Institute of Fundamental Research, Bangalore, Karnataka, India

[*]*For correspondence: tung.le@jic.ac.uk*

ABSTRACT
Proper chromosome segregation is essential in all living organisms. The ParA-ParB-*parS* system is widely employed for chromosome segregation in bacteria. Previously, we showed that *Caulobacter crescentus* ParB requires cytidine triphosphate to escape the nucleation site *parS* and spread by sliding to the neighboring DNA. Here, we provide the structural basis for this transition from nucleation to spreading by solving co-crystal structures of a C-terminal domain truncated *C. crescentus* ParB with *parS* and with a CTP analog. Nucleating ParB is an open clamp, in which *parS* is captured at the DNA-binding domain (the DNA-gate). Upon binding CTP, the N-terminal domain (NTD) self-dimerizes to close the NTD-gate of the clamp. The DNA-gate also closes, thus driving *parS* into a compartment between the DNA-gate and the C-terminal domain. CTP hydrolysis and/or the release of hydrolytic products may subsequently re-open the gates. Overall, we suggest a CTP-operated gating mechanism that regulates ParB nucleation and spreading.

KEYWORDS: chromosome segregation, ParA-ParB-*parS*, nucleation, spreading, CTP, and molecular gates.

bioRxiv preprint doi: https://doi.org/10.1101/816959; this version posted May 5, 2021. The copyright holder for this preprint (which was not certified by peer review) is the author/funder, who has granted bioRxiv a license to display the preprint in perpetuity. It is made available under aCC-BY 4.0 International license.

INTRODUCTION

Proper chromosome segregation is essential in all domains of life. In most bacterial species, faithful chromosome segregation is mediated by the tripartite ParA-ParB-*parS* system[1–11]. ParB, a CTPase and DNA-binding protein, nucleates on *parS* before spreading to adjacent non-specific DNA to form a higher-order nucleoprotein complex[1,12–17]. The ParB-DNA nucleoprotein complex stimulates the ATPase activity of ParA, driving the movement of the *parS* locus (and subsequently, the whole chromosome) to the opposite pole of the cell[18–23]. ParB spreads by sliding along the DNA, in a manner that depends on the binding of a co-factor, cytidine triphosphate (CTP)[24–26]. A co-crystal structure of a C-terminal domain truncated *Bacillus subtilis* ParB (ParBΔCTD) together with CDP showed the nucleotide to be sandwiched between adjacent subunits, thus promoting their dimerization[26]. A similar arrangement was seen in the co-crystal structure of an N-terminal domain truncated version of the *Myxococcus xanthus* ParB homolog, PadC, bound to CTP[25]. Self-dimerization at the N-terminal domain (NTD) of *B. subtilis* ParB creates a clamp-like molecule that enables DNA entrapment[26]. Biochemical studies with *M. xanthus* and *C. crescentus* ParBs showed that CTP facilitates the dissociation of ParB from *parS*, thereby switching ParB from a nucleating mode to a sliding mode[24,25]. ParB can hydrolyze CTP to CDP and inorganic phosphate[24–26], however hydrolysis is not required for spreading since ParB in complex with a non-hydrolyzable CTP analog (CTPɣS) can still self-load and slide on DNA[24,26]. Furthermore, *M. xanthus* PadC does not possess noticeable CTPase activity[25]. As such, the role of CTP hydrolysis in bacterial chromosome segregation is not yet clear.

Here, we solve co-crystal structures of a C-terminal domain truncated *C. crescentus* ParB in complex with either *parS* or CTPɣS to better understand the roles of CTP binding and hydrolysis. Consistent with the previous report[26], the NTDs of *C. crescentus* ParB also self-dimerize upon binding to nucleotides, thus closing a molecular gate at this domain (the NTD-gate). Furthermore, the two opposite DNA-binding domains (DBD) move closer together to close a second molecular gate (the DNA-gate). We provide evidence that the CTP-induced closure of the DNA-gate drives *parS* DNA from the DBD into a 20-amino-acid long compartment between the DNA-gate and the C-terminal domain, thus explaining how CTP binding enables ParB to escape the high-affinity *parS* site to spread while still entrapping DNA. Lastly, we identify and characterize a ParB "clamp-locked" mutant that is defective in CTP hydrolysis but otherwise competent in gate closing, suggesting a role for CTP hydrolysis/release of hydrolytic products in the re-opening ParB gates. Collectively, we suggest a CTP-operated gating mechanism that regulates ParB nucleation and spreading in *C. crescentus*.

RESULTS

Co-crystal structure of a *C. crescentus* ParBΔCTD-*parS* complex reveals an open conformation at the NTD

We sought to solve a co-crystal structure of *C. crescentus* ParB nucleating at *parS*. After screening several constructs with different lengths of ParB and *parS*, we obtained crystals of a 50 amino acid C-terminally truncated ParB in complex with a 22-bp *parS* DNA (Figure 1). This protein variant lacks the CTD reponsible for ParB dimerization (Figure 1A)[27]. Diffraction data for the ParBΔCTD-*parS* co-crystal were collected to 2.9 Å resolution, and the structure was solved by molecular replacement (see Materials and Methods). The asymmetric unit contains four copies of ParBΔCTD and two copies of the *parS* DNA (Figure 1-figure supplement 1A-B).

Each ParBΔCTD subunit consists of an NTD (helices α1-α4 and sheets β1-β4) and a DBD (helices α5-α10) (Figure 1B). Each ParBΔCTD binds to a half *parS* site but there is no protein-protein contact between the two adjacent subunits (Figure 1B). We previously reported a 2.4 Å co-crystal structure of the DBD of *C. crescentus* ParB bound to *parS*[28] and elucidated the molecular basis for specific *parS* recognition, hence we focus on the conformation of the NTD here instead. We observed that helices α3 and α4 are packed towards the DBD and are connected to the rest of the NTD via an α3-β4 loop (Figure 1B-C). While the DBD and helices α3-α4 are near identical between the two ParBΔCTD subunits (RMSD=0.19 Å, Figure 1C), the rest of the NTD, from α1 to β4, adopts notably different conformations in the two subunits (Figure 1C-D). Specifically, NTDs (α1-β4) from the two ParBΔCTD subunits are related by a rotation of approximately 80°, due to changes in a flexible

bioRxiv preprint doi: https://doi.org/10.1101/816959; this version posted May 5, 2021. The copyright holder for this preprint (which was not certified by peer review) is the author/funder, who has granted bioRxiv a license to display the preprint in perpetuity. It is made available under aCC-BY 4.0 International license.

loop in between α3 and β4 (Figure 1D). Furthermore, by superimposing the *C. crescentus* ParBΔCTD-*parS* structure onto that of *Helicobacter pylori*[29], we observed that the NTDs of ParB from both species can adopt multiple alternative orientations (Figure1-figure supplement 2). Taken together, these observations suggest that the ability of the NTD to adopt multiple open conformations is likely a general feature of nucleating ParB.

Co-crystal structure of a *C. crescentus* ParBΔCTD-CTPɣS complex reveals a closed conformation at the NTD

Next, to gain insight into the spreading state of ParB, we solved a 2.7 Å resolution structure of *C. crescentus* ParBΔCTD in complex with CTPɣS (see Materials and Methods). At this resolution, it was not possible to assign the position of the ligand sulfur atom. Indeed, the placement of the sulfur atom relative to the terminal phosphorus atom may vary from one ligand to the next in the crystal leading to an averaging of the electron density. Hence, we modeled CTP, instead of CTPɣS, into the electron density (Figure 2 and Figure 2-figure supplement 1). The asymmetric unit contains two copies of ParBΔCTD, each with a CTPɣS molecule and a coordinated Mg^{2+} ion bound at the NTD (Figure 2A). In contrast to the open conformation of the ParBΔCTD-*parS* structure, nucleotide-bound NTDs from opposite subunits self-dimerize (with an interface area of 2111 $Å^2$, as determined by PISA[30]), thus adopting a closed conformation (Figure 2A). Multiple CTPɣS-contacting residues also directly contribute to the NTD self-dimerization interface (summarized in Figure 2-figure supplement 2), indicating a coupling between nucleotide binding and self-dimerization. Furthermore, the *C. crescentus* ParBΔCTD-CTPɣS structure is similar to that of the CDP-bound *B. subtilis* ParBΔCTD (RMSD=1.48 Å) and the CTP-bound *M. xanthus* PadCΔNTD (RMSD=2.23 Å) (Figure 2-figure supplement 3A), suggesting that the closed conformation at the NTD is structurally conserved in nucleotide-bound ParB/ParB-like proteins.

Each CTPɣS molecule is sandwiched between helices α1, α2, α3 from one subunit and helix α3' from the opposite subunit (Figure 2B). Ten amino acids form hydrogen-bonding contacts with three phosphate groups of CTPɣS, either directly or via the coordinated Mg^{2+} ion (Figure 2C). These phosphate-contacting residues are referred to as P-motifs 1 to 3, respectively (P for phosphate motif, Figure 2C). Four amino acids at helix α1 and the α1-β2 intervening loop provide hydrogen-bonding interactions to the cytosine ring, hence are termed the C-motif (C for cytosine motif, Figure 2C). Lastly, six additional residues contact the ribose moiety and/or the pyrimidine moiety via hydrophobic interactions (Figure 2C). Nucleotide-contacting residues in *C. crescentus* ParB and their corresponding amino acids in ParB/ParB-like homologs are summarized in Figure 2-figure supplement 2 and Figure 2-figure supplement 3B. The C-motif forms a snug fit to the pyrimidine moiety, thus is incompatible with larger purine moieties such as those from ATP or GTP. Hydrogen-bonding contacts from the G79 main chain and the S74 side chain to the amino group at position 4 of the cytosine moiety further distinguish CTP from UTP (Figure 2C). Taken all together, our structural data are consistent with the known specificity of *C. crescentus* ParB for CTP[24].

Conformational changes between the nucleating and the spreading state of *C. crescentus* ParB

A direct comparison of the *C. crescentus* ParBΔCTD-*parS* structure to the ParBΔCTD-CTPɣS structure further revealed the conformational changes upon nucleotide binding. In the nucleating state, as represented by the ParBΔCTD-*parS* structure, helices α3 and α4 from each subunit bundle together (32° angle between α3 and α4, Figure 3). However, in the spreading state, as represented by the ParBΔCTD-CTPɣS structure, α3 swings outwards by 101° to pack itself with α4' from the opposing subunit (Figure 3). Nucleotide binding most likely facilitates this "swinging-out" conformation since both α3 and the α3-α4 loop i.e. P-motif 3 make numerous contacts with the bound CTPɣS and the coordinated Mg^{2+} ion (Figure 2C). The reciprocal exchange of helices ensures that the packing in the α3-α4 protein core remains intact, while likely driving the conformational changes for the rest of the NTD as well as the DBD (Figure 4A). Indeed, residues 44-121 at the NTD rotate wholesale by 94° to dimerize with their counterpart from the opposing subunit (Figure 4A and Figure 4-figure supplement 1A). Also, residues 161-221 at the DBD rotate upward by 26° in a near rigid-body movement (Figure 4A and Figure 4-figure supplement 1A). As the result, the opposite DBDs are closer together in the spreading state

bioRxiv preprint doi: https://doi.org/10.1101/816959; this version posted May 5, 2021. The copyright holder for this preprint (which was not certified by peer review) is the author/funder, who has granted bioRxiv a license to display the preprint in perpetuity. It is made available under aCC-BY 4.0 International license.

(inter-domain distance = ~27 Å) than in the nucleating state (inter-domain distance = ~36 Å) (Figure 4-figure supplement 1B). By overlaying the CTPγS-bound structure onto the *parS* DNA complex, it is clear that the DBDs in the spreading state clash severely with DNA, hence are no longer compatible with *parS* DNA binding (Figure 4B). Our structural data are therefore consistent with the previous finding that CTP decreases *C. crescentus* ParB nucleation on *parS* or liberates pre-bound ParB from *parS* site[24]. Overall, we suggest that CTP binding stabilizes a conformation that is incompatible with DNA-binding and that this change might facilitate ParB escape from the high-affinity nucleation *parS* site.

C. crescentus ParB entraps *parS* DNA in a compartment between the DBD and the CTD in a CTP-dependent manner

To verify the CTP-dependent closed conformation of ParB, we performed site-specific crosslinking of purified proteins using a sulfhydryl-to-sulfhydryl crosslinker bismaleimidoethane (BMOE)[26]. Residues Q35, L224, and I304 at the NTD, DBD, and CTD, respectively (Figure 5A) were substituted individually to cysteine on an otherwise cysteine-less ParB (C297S) background[24], to create ParB variants where symmetry-related cysteines become covalently linked if they are within 8 Å of each other (Figure 5B). We observed that the crosslinking of both ParB (Q35C) and ParB (L224C) were enhanced ~2.5 to 3-fold in the presence of *parS* DNA and CTP (Figure 5B), consistent with CTP favoring a conformation when the NTD and the DBD are close together. In contrast, ParB (I304C) crosslinked independently of CTP or *parS* (Figure 5B), supporting the known role of the CTD as a primary dimerization domain[27,31].

Previously, Soh *et al* (2019) showed that *B. subtilis* ParB-CTP forms a protein clamp that entraps DNA[26], however the location of DNA within the clamp is not yet clear. To locate such DNA-entrapping compartment, we employed a double crosslinking assay[26] while taking advantage of the availability of crosslinkable cysteine residues in all three domains of *C. crescentus* ParB (Figure 5A). A *C. crescentus* ParB variant with crosslinkable NTD and CTD interfaces (Q35C I304C) was first constructed and purified (Figure 5C). ParB (Q35C I304C) could form high molecular weight (HMW) species near the top of the polyacrylamide gel in the presence of CTP, a 3-kb *parS* plasmid, and the crosslinker BMOE (Lane 7, Figure 5C-Left panel). The HMW smear on the polyacrylamide gel contained both protein and DNA as apparent from a dual staining with Coomassie and Sybr Green (Figure 5C-Left panel). Slowly migrating DNA-stained bands were also observed when resolving on an agarose gel (Figure 5C-Right panel). The HMW smear most likely contained DNA-protein catenates between a circular *parS* plasmid and a denatured but otherwise circularly crosslinked ParB (Q35C I304C) polypeptide. Indeed, a post-crosslinking treatment with Benzonase, a non-specific DNA nuclease (Lane 8, Figure 5C-Left panel) or the use of a linear *parS* DNA (Lane 4, Figure 5C-Left panel) eliminated the HMW smear, presumably by unlinking the DNA-protein catenates. Lastly, the HMW smear was not observed when a plasmid containing a scrambled *parS* site was used (Lane 10, Figure 5C-Left panel) or when CTP was omitted from the crosslinking reaction (Lane 6, Figure 5C-Left panel), indicating that the DNA entrapment is dependent on *parS* and CTP. Collectively, these experiments demonstrate that as with the *B. subtilis* ParB homolog, *C. crescentus* ParB is also a CTP-dependent molecular clamp that can entrap *parS* DNA in between the NTD and the CTD.

Employing the same strategy, we further narrowed down the DNA-entrapping compartment by constructing a ParB (L224C I304C) variant in which both the DBD and the CTD are crosslinkable (Figure 4D). We found that crosslinked ParB (L224C I304C) also entrapped circular plasmid efficiently in a *parS*- and CTP-dependent manner, as judged by the appearance of the HMW smear near the top of the gel (Lane7, Figure 5D-Left panel). By contrast, ParB (Q35C L224C) that has both the NTD and the DBD crosslinkable, was unable to entrap DNA in any tested condition (Figure 5-figure supplement 1). We therefore hypothesized that ParB clamps entrap DNA within a compartment created by a 20-amino-acid linker in between the DBD and the CTD. To investigate further, we constructed a ParB (L224C I304C)TEV variant, in which a TEV protease cleavage site was inserted within the DBD-CTD linker (Figure 5-figure supplement 2A). Again, ParB (L224C I304C)TEV entrapped a circular *parS* plasmid efficiently in the presence of CTP (the HMW smear on lane 7, Figure 5-figure supplement 2A). However, a

bioRxiv preprint doi: https://doi.org/10.1101/816959; this version posted May 5, 2021. The copyright holder for this preprint (which was not certified by peer review) is the author/funder, who has granted bioRxiv a license to display the preprint in perpetuity. It is made available under aCC-BY 4.0 International license.

post-crosslinking treatment with TEV protease eliminated such HMW smear, presumably by creating a break in the polypeptide through which a circular plasmid could escape (Lane 8, Figure 5-figure supplement 2A). Lastly, we extracted crosslinked ParB (L224C I304C) from gel slides that encompassed the HMW smear, and electrophoresed the eluted proteins again on a denaturing gel to find a single band that migrated similarly to a double-crosslinked protein (Lane 9, Figure 5-figure supplement 2B). Therefore, our results suggest that a ParB dimer, rather than ParB oligomers, is the major species that entraps DNA. Taken together, we suggest that *C. crescentus* ParB dimer functions as a molecular clamp that entraps *parS*-containing DNA within a DBD-CTD compartment upon CTP binding.

C. crescentus ParB (E102A) is a clamp-locked mutant that is defective in clamp re-opening

Next, we investigated the potential role(s) of CTP hydrolysis. Hydrolysis is unlikely to be required for DNA entrapment and translocation since ParB in complex with CTPɣS can still self-load and slide on DNA[24,26]. *M. xanthus* ParB (N172A) and *B. subtilis* ParB (N112S) mutants, which bind but cannot hydrolyze CTP, failed to form higher-order protein-DNA complexes inside the cells[25,26]. However, these ParB variants are already impaired in NTD self-dimerization[26], hence the mechanistic role of CTP hydrolysis is still unclear. We postulated that creation of a ParB variant defective in CTP hydrolysis but otherwise competent in NTD self-dimerization, would enable us to investigate the possible role of CTP hydrolysis. To this end, we performed alanine scanning mutagenesis on the CTP-binding pocket of *C. crescentus* ParB (Figure 2C). Eleven purified ParB variants were assayed for CTP binding by a membrane-spotting assay (DRaCALA) (Figure 6A), and for CTP hydrolysis by measuring the releasing rate of inorganic phosphate (Figure 6B). Moreover, their propensity for NTD self-dimerization was also analyzed by crosslinking with BMOE (Figure 6C and Figure 6-figure supplement 1). Lastly, their ability to nucleate, slide, and entrap a closed *parS* DNA substrate was investigated by a bio-layer interferometry (BLI) assay (Figure 6D and Figure 6-figure supplement 2A). Immobilizing a dual biotin-labeled DNA on a streptavidin-coated BLI surface created a closed DNA substrate that can be entrapped by ParB-CTP clamps (Figure 6-figure supplement 2A)[24]. The BLI assay monitors wavelength shifts resulting from changes in the optical thickness of the probe surface during the association/dissociation of ParB with a closed DNA substrate in real-time (Figure 6-figure supplement 2).

Overall, we identified several distinct classes of ParB mutants:

(i) Class I: ParB (R60A), (R103A), (R104A), (R139A), (N136A), (G79S), and (S74A) did not bind or bound radiolabeled CTP only weakly (Figure 6A), thus also showed weak to no CTP hydrolysis (Figure 6B) or clamp-closing activity (Figure 6C-D).

(ii) Class II: ParB (Q58A) and (E135A) that are competent in CTP-binding (Figure 6A), but defective in CTP hydrolysis (Figure 6B) and in entrapping a closed *parS* DNA substrate (Figure 6D). We noted that ParB (Q58A) and ParB (E135A) had an elevated crosslinking efficiency even in the absence of CTP (Figure 6C) but did not result in a wild-type level of DNA entrapment (Figure 6D).

(iii) Class III: ParB (E102A) did not hydrolyze CTP (Figure 6B) but nevertheless bound CTP efficiently (Figure 6A) to self-dimerize at the NTD and to entrap DNA to the same level as ParB (WT) at all CTP concentrations (Figure 6C-D).

Upon a closer inspection of the BLI sensorgrams (Figure 6-figure supplement 2B and Figure 7), we noted that the entrapped ParB (E102A) did not noticeably dissociate from a closed DNA substrate when the probe was returned to a buffer-only solution (Dissociation phase, $k_{off} = 8.0 \times 10^{-4} \pm 1.9 \times 10^{-4}\ s^{-1}$, Figure 6-figure supplement 2B and Figure 7). By contrast, entrapped ParB (WT) dissociated approx. 15-fold faster into buffer ($k_{off} = 1.2 \times 10^{-2} \pm 3.7 \times 10^{-4}\ s^{-1}$). Further experiments showed that DNA-entrapment by ParB (E102A), unlike ParB (WT), is more tolerable to high-salt solution (up to 1 M NaCl, Figure 7A). Nevertheless, ParB (E102A)-CTP could not accumulate on a BamHI-restricted open DNA substrate (Figure 7B-C)[24], suggesting that ParB (E102A)-CTP, similar to ParB (WT), also form a closed clamp that runs off an open DNA end. Collectively, our results suggest that *parS* DNA and CTP induced a

bioRxiv preprint doi: https://doi.org/10.1101/816959; this version posted May 5, 2021. The copyright holder for this preprint (which was not certified by peer review) is the author/funder, who has granted bioRxiv a license to display the preprint in perpetuity. It is made available under aCC-BY 4.0 International license.

stably closed clamp conformation of ParB (E102A) *in vitro*.

To investigate the function of ParB (E102A) *in vivo*, we expressed a FLAG-tagged version of *parB* (E102A) from a vanillate-inducible promoter (P_{van}) in a *C. crescentus* strain where the native *parB* was under the control of a xylose-inducible promoter (P_{xyl}) (Figure 8A). Cells were depleted of the native ParB by adding glucose for 4 hrs, subsequently vanillate was added for another hour before cells were fixed with formaldehyde for ChIP-seq. Consistent with the previous report[11], the ChIP-seq profile of FLAG-ParB (WT) showed a ~10-kb region of enrichment above background with clearly defined peaks that correspond to the positions of *parS* sites (Figure 8A). By contrast, the ChIP-seq profile of FLAG-ParB (E102A) is reduced in height but is notably more extended than the profile of FLAG-ParB (WT) (shaded area, Figure 8A). The instability of FLAG-ParB (E102A) *in vivo*, hence the reduced protein level (Figure 8-figure supplement 1), might explain the lower height of its ChIP-seq profile (Figure 8). However, the more extended profile of FLAG-ParB (E102A) is likely due to a stably closed clamp formation of ParB (E102) that enables this variant to persist, and thus sliding further away from the loading site *parS in vivo*.

Altogether, the "clamp-locked" phenotype of ParB (E102A) implies a possible role of CTP hydrolysis and/or the release of hydrolytic products in re-opening wild-type ParB clamp to discharge DNA. Lastly, we noted that the producing ParB (E102A) could not rescue cells with depleted ParB (WT) (Figure 8B). However, due to the caveat of a lower ParB (E102A) protein level (Figure 8-figure supplement 1), we could not reliably attribute its lethal phenotype to the defective CTP hydrolysis alone.

DISCUSSION

In this study, we provide structural insights into the nucleating and sliding states of *C. crescentus* ParB. Nucleating ParB is an open clamp in which *parS* DNA is held tightly (nM affinity)[11] at the DBD. The NTDs of nucleating ParB can adopt multiple alternative conformations, and crucially there is no contact between opposing NTDs. We liken this conformation of the NTD to that of an open gate (NTD-gate), through which *parS* DNA might gain access to the DNA-binding domain (Figure 9). In the sliding state, CTP promotes the self-dimerization of the NTDs, thus closing the NTD-gate (Figure 9). Opposing DBDs also move approximately 10 Å closer together, bringing about a conformation that is DNA incompatible. Again, we liken this conformation of the DBDs to that of a closed gate (DNA-gate) (Figure 9). Overall, the DNA-gate closure explains how CTP binding might switch ParB from a nucleating to a sliding state.

Our data suggest that the closure of the two gates drives *parS* DNA into a compartment in between the DBD and the CTD. Previously, Soh *et al*. (2019) compared the *B. subtilis* ParBΔCTD-CDP co-crystal structure to that of a *H. pylori* ParBΔCTD-*parS* complex and proposed that DNA must be entrapped in the DBD-CTD compartment[26]. Here, the available structures of nucleating and sliding ParB from the same bacterial species enabled us to introduce a crosslinkable cysteine (L224C) at the DBD, and subsequently provided a direct evidence that the DBD-CTD compartment is the DNA-entrapping compartment. The linker that connects the DBD and the CTD together is not conserved in amino acid sequence among chromosomal ParB orthologs (Figure 2-figure supplement 2), however we noted that the linker is invariably ~20 amino acid in length and positively charge lysines are over-represented (Figure 2-figure supplement 2). The biological significance of the linker length and its lysines, if any, is currently unknown. However, it is worth noting that a human PCNA clamp was proposed to recognize DNA via lysine-rich patches lining the clamp channel, and that these lysine residues help PCNA to slide by tracking the DNA backbone[32]. Investigating whether lysine residues in the DBD-CTD linker of ParB have a similar role is an important subject for the future.

If not already bound on DNA, the closed ParB clamp presumably cannot self-load onto *parS* owing to its inaccessible DBD. In this study, we showed that *parS* DNA promotes the CTP-dependent NTD-gate closure (Figure 5B), thus is likely a built-in mechanism to ensure gate closure results in a productive DNA entrapment. However, the molecular basis for the *parS*-enhanced gate closure remains unclear due to the lack of a crystal structure of *C. crescentus* apo-ParB, despite our extensive efforts.

bioRxiv preprint doi: https://doi.org/10.1101/816959; this version posted May 5, 2021. The copyright holder for this preprint (which was not certified by peer review) is the author/funder, who has granted bioRxiv a license to display the preprint in perpetuity. It is made available under aCC-BY 4.0 International license.

CTP functions as a molecular latch that stabilizes the closure of the NTD-gate of ParB. Here, we provide evidence that CTP hydrolysis might contribute to re-opening the closed NTD-gate. A previous structure of a *B. subtilis* ParBΔCTD-CDP complex also has its NTD-gate closed (CTP was hydrolyzed to CDP during the crystallization)[26], hence it is likely that both CTP hydrolysis and the subsequent release of hydrolytic products are necessary to re-open the gates. However, ParB has a weak to negligible affinity for CDP, hence the CDP-bound ParB species might be short-lived in solution and might not play a significant biological role. Once the clamp is re-opened, entrapped DNA might escape via the same route that it first enters. Other well-characterized DNA clamps, for example, type II topoisomerases open their CTD to release trapped DNA. However, the CTDs of ParB are stably dimerized independently of *parS* and CTP (Figure 5B), hence we speculate that the CTD of ParB is likely to be impassable to the entrapped DNA. The released ParB clamp might re-nucleate on *parS* and bind CTP to close the gate, hence restarting the nucleation and sliding cycle. Such a recycling mechanism might provide a biological advantage since a ParB clamp once closed could otherwise become stably trapped on DNA and thus eventually diffuse too far from the *parS* locus, as evidenced by the E102A variant that is defective in CTP hydrolysis (Figure 8A).

The CTP-bound structure of a *M. xanthus* ParB-like protein, PadC, was solved to a high resolution (1.7 Å), however, PadC does not possess noticeable CTPase activity[25]. A co-crystal structure of *B. subtilis* ParB with CDP was also solved to a high resolution (1.8 Å) but represents a post-hydrolysis state instead. Lastly, our CTPγS-bound *C. crescentus* ParB crystals diffracted to 2.7 Å, thus preventing water molecules, including a potential catalytic water, from being assigned with confidence. Therefore, the mechanism of CTP hydrolysis by a ParB CTPase remains unresolved. Nevertheless, based on our alanine scanning experiment (Figure 8), we speculate that Q58 (P-motif 1) and E102 (P-motif 2) might be involved in the catalytic mechanism of *C. crescentus* ParB. Supporting this view, we noted that an equivalent Q37 in *B. subtilis* ParB does not contact the hydrolytic product CDP, and this residue is not conserved in the catalytic-dead *M. xanthus* PadC (F308, which does not contact CTP, occupies this position in PadC instead) (Figure 2-figure supplement 3). E102 is also not conserved in M. *xanthus* PadC (F348 occupies this equivalent position) (Figure 2-figure supplement 3). Given that ParB is the founding member of a new CTPase protein family[25,26], further studies are needed to fully understand the molecular mechanism of CTP hydrolysis so that the knowledge gained might be generalized to other CTPases.

FINAL PERSPECTIVES

In this study, we provide a structural basis for a CTP-operated gating mechanism that regulate the opening and closing of the DNA-clamp ParB. CTP functions as a molecular switch that converts ParB from a nucleating to a sliding and DNA-entrapping state. Overall, CTP is crucial for the formation of the higher-order ParB-DNA complex *in vivo*, and ultimately for the faithful chromosome segregation in the majority of bacterial species. ATP and GTP switches are extensively used to control conformations and functions of proteins in a wide range of biological processes. However, CTP switches have rarely been found in biology so far. It is tempting to speculate that CTP switches may also be widespread in biology and await discovery. Moreover, it will be interesting to establish if evolution has also exploited this framework of CTP-induced conformational changes to regulate other diverse biological processes.

ACKNOWLEDGEMENTS

This study was funded by the Royal Society University Research Fellowship (UF140053), BBSRC grant (BB/P018165/1 and BBS/E/J/000PR9791), and Royal Society Research Grant (RG150448) (to T.B.K.L) and a DST-SERB CRG grant 2019/003321 (to A.B). We thank Diamond Light Source for access to beamlines I04-1 and I03 under proposals MX13467 and MX18565 with support from the European Community's Seventh Framework Program (FP7/2007–2013) under Grant Agreement 283570 (BioStruct-X).

ACCESSION NUMBER

The accession number for the sequencing data reported in this paper is **GSE168968**. Atomic coordinates for protein crystal structures reported in this paper were deposited in the RCSB Protein Data Bank with the accession number **6T1F** and **7BM8**. All data are open to the public upon the deposition of this preprint.

bioRxiv preprint doi: https://doi.org/10.1101/816959; this version posted May 5, 2021. The copyright holder for this preprint (which was not certified by peer review) is the author/funder, who has granted bioRxiv a license to display the preprint in perpetuity. It is made available under aCC-BY 4.0 International license.

MATERIALS AND METHODS

Strains, media and growth conditions

Escherichia coli and *Caulobacter crescentus* were grown in LB and PYE, respectively. When appropriate, media were supplemented with antibiotics at the following concentrations (liquid/solid media for *C. crescentus*; liquid/solid media for *E. coli* (µg/mL)): carbenicillin (*E. coli* only: 50/100), chloramphenicol (1/2; 20/30), kanamycin (5/25; 30/50), and oxytetracycline (1/2; 12/12).

Plasmids and strains construction

All strains, plasmids, and primers used in this study are listed in Supplementary File S1.

Construction of pET21b::parBΔCTD-(his)$_6$

The coding sequence of a C-terminally truncated *C. crescentus* ParB (ParBΔCTD, lacking the last 50 amino acids) was amplified by PCR using primers NdeI-Ct-ParB-F and HindIII-Ct-ParB-R, and pET21b::*parB-(his)$_6$*[18] as template. The pET21b plasmid backbone was generated via a double digestion of pET21b::*parB-(his)$_6$* with NdeI and HindIII. The resulting backbone was subsequently gel-purified and assembled with the PCR-amplified fragment of *parBΔCTD* using a 2x Gibson master mix (NEB). Gibson assembly was possible owing to a 23-bp sequence shared between the NdeI-HindIII-cut pET21b backbone and the PCR fragment. These 23-bp regions were incorporated during the synthesis of primers NdeI-Ct-ParB-F and HindIII-Ct-ParB-R. The resulting plasmids were sequence verified by Sanger sequencing (Eurofins, Germany).

Construction of pET21b::parB-(his)$_6$ (WT and mutants)

DNA fragments containing mutated *parB* genes (*parB**) were chemically synthesized (gBlocks, IDT). The NdeI-HindIII-cut pET21b plasmid backbone and *parB** gBlocks fragments were assembled together using a 2x Gibson master mix (NEB). Gibson assembly was possible owing to a 23-bp sequence shared between the NdeI-HindIII-cut pET21b backbone and the gBlocks fragment. The resulting plasmids were sequenced verified by Sanger sequencing (Genewiz, UK).

pUC57::attL1-parB (WT/mutant)-attL2

The coding sequences of *C. crescentus* ParB (WT/mutants) were amplified by PCR and Gibson assembled into plasmid pUC57::attL1-*parB* (WT/mutants)-attL2 so that *parB* is flanked by phage attachment sites attL1 and attL2 i.e. Gateway cloning compatible. Correct mutations were verified by Sanger sequencing (Genewiz, UK).

pMT571-1xFLAG-DEST

Plasmid pMT571[33] was first digested with NdeI and NheI. The plasmid backbone was gel-purified and eluted in 50 µL of water. The FLAG-attR1-ccdB-chloramphenicol^R-attR2 cassette was amplified by PCR using primers P1952 and P1953, and pML477 as template. The resulting PCR fragment and the NdeI-NheI-cut pMT571 were assembled together using a 2xGibson master mix (NEB). Gibson assembly was possible owing to a 23 bp sequence shared between the two DNA fragments. These 23 bp regions were incorporated during the primer design to amplify the FLAG-attR1-ccdB-chloramphenicol^R-attR2 cassette. The resulting plasmid was sequence verified by Sanger sequencing (Eurofins, Germany).

pMT571-1xFLAG::ParB (WT/mutants)

The *parB* (WT/mutant) genes were recombined into a Gateway-compatible destination vector pMT571-1xFLAG-DEST via LR recombination reaction (Invitrogen). For LR recombination reactions: 1 µL of purified pUC57::attL1-*parB* (WT/mutant)-attL2 was incubated with 1 µL of the destination vector pMT571-1xFLAG-DEST, 1 µL of LR Clonase II master mix, and 2 µL of water in a total volume of 5 µL. The reaction was incubated for an hour at room temperature before being introduced into *E. coli* DH5α cells by heat-shock transformation. Cells were then plated out on LB agar + tetracycline. Resulting colonies were restruck onto LB agar + carbenicillin and LB agar + tetracycline. Only colonies that survived on LB + tetracycline plates were subsequently used for culturing and plasmid extraction.

Strains MT148 + pMT571-1xFLAG::ParB (WT/mutants)

Electro-competent *C. crescentus* (NA1000) cells were electroporated with pMT571-1xFLAG::ParB (WT/mutants) plasmid to allow for a single integration at the *vanA* locus. The correct integration was verified by PCR, and ΦCr30 phage lysate was prepared from this strain. Subsequently, *van*::P$_{van}$*-1xflag-parB* (WT/mutant), marked by a tetracycline^R

bioRxiv preprint doi: https://doi.org/10.1101/816959; this version posted May 5, 2021. The copyright holder for this preprint (which was not certified by peer review) is the author/funder, who has granted bioRxiv a license to display the preprint in perpetuity. It is made available under aCC-BY 4.0 International license.

cassette, was transduced by phage ΦCr30 into MT148[34].

Protein overexpression and purification

Plasmid pET21b::*parBΔCTD-(his)*$_6$ was introduced into *E. coli* Rosetta pRARE competent cells (Novagen) by heat-shock transformation. Forty mL overnight culture was used to inoculate 4 L of LB medium + carbenicillin + chloramphenicol. Cells were grown at 37˚C with shaking at 250 rpm to an OD_{600} of ~0.4. The culture was then left in the cold room to cool to 28˚C before isopropyl-β-D-thiogalactopyranoside (IPTG) was added at a final concentration of 0.5 mM. The culture was shaken for an additional 3 hours at 30ºC before cells were pelleted by centrifugation. Pelleted cells were resuspended in a buffer containing 100 mM Tris-HCl pH 8.0, 300 mM NaCl, 10 mM Imidazole, 5% (v/v) glycerol, 1 µL of Benzonase nuclease (Merck), 10 mg of lysozyme (Merck), and an EDTA-free protease inhibitor tablet (Merck). Cells were further lyzed by sonification (10 cycles of 15 s with 10 s resting on ice in between each cycle). The cell debris was removed through centrifugation at 28,000 g for 30 minutes and the supernatant was filtered through a 0.45 µm sterile filter (Sartorius). The protein was then loaded into a 1-mL HiTrap column (GE Healthcare) that had been pre-equilibrated with buffer A [100 mM Tris-HCl pH 8.0, 300 mM NaCl, 10 mM Imidazole, and 5% (v/v) glycerol]. Protein was eluted from the column using an increasing (10 mM to 500 mM) Imidazole gradient in the same buffer. ParBΔCTD-containing fractions were pooled and diluted to a conductivity of 16 mS/cm before being loaded onto a 1-mL Heparin HP column (GE Healthcare) that had been pre-equilibrated with 100 mM Tris-HCl pH 8.0, 25 mM NaCl, and 5% (v/v) glycerol. Protein was eluted from the Heparin column using an increasing (25 mM to 1 M NaCl) salt gradient in the same buffer. ParBΔCTD fractions were pooled and analyzed for purity by SDS-PAGE. Glycerol was then added to ParBΔCTD fractions to a final volume of 10% (v/v), followed by 10 mM EDTA and 1 mM DTT. The purified ParBΔCTD was subsequently aliquoted, snap frozen in liquid nitrogen, and stored at -80˚C. ParBΔCTD that was used for X-ray crystallography was further polished via a gel-filtration column. To do so, purified ParBΔCTD was concentrated by centrifugation in an Amicon Ultra-15 3-kDa cut-off spin filters (Merck) before being loaded into a Superdex-200 gel filtration column (GE Healthcare). The gel filtration column was pre-equilibrated with buffer containing 10 mM Tris-HCl pH 8.0 and 250 mM NaCl. ParBΔCTD fractions were then pooled and analyzed for purity by SDS-PAGE.

Other C-terminally His-tagged ParB mutants were purified using HIS-Select® Cobalt gravity flow columns as described previously[28]. Purified proteins were desalted using a PD-10 column (Merck), concentrated using an Amicon Ultra-4 10 kDa cut-off spin column (Merck), and stored at -80˚C in a storage buffer [100 mM Tris-HCl pH 8.0, 300 mM NaCl, and 10% (v/v) glycerol]. Purified ParB mutants that were used in BMOE crosslinking experiments were buffer-exchanged and stored in a storage buffer supplemented with TCEP instead [100 mM Tris-HCl pH 7.4, 300 mM NaCl, 10% (v/v) glycerol, and 1 mM TCEP].

DNA preparation for crystallization, EnzCheck phosphate release assay, and differential radical capillary action of ligand assay (DRaCALA)

A 22-bp palindromic single-stranded DNA fragment (*parS*: GGATGTTTCACGTGAAACA TCC) [100 µM in 1 mM Tris-HCl pH 8.0, 5 mM NaCl buffer] was heated at 98°C for 5 minutes before being left to cool down to room temperature overnight to form 50 µM double-stranded *parS* DNA. The core sequence of *parS* is underlined.

Protein crystallization, structure determination, and refinement

Crystallization screens for the *C. crescentus* ParBΔCTD-*parS* complex were set up in sitting-drop vapour diffusion format in MRC2 96-well crystallization plates with drops comprised of 0.3 µL precipitant solution and 0.3 µL of protein-DNA complex, and incubated at 293 K. His-tagged ParBΔCTD (approx. 10 mg/mL) was mixed with a 22-bp *parS* duplex DNA at a molar ratio of 2:1.2 (protein monomer:DNA) in buffer containing 10 mM Tris-HCl pH 8.0 and 250 mM NaCl. The ParBΔCTD-*parS* crystals grew in a solution containing 20.5% (w/v) PEG 3350, 260 mM magnesium formate, and 10% (v/v) glycerol. After optimization of an initial hit, suitable crystals were cryoprotected with 20% (v/v) glycerol and mounted in Litholoops (Molecular Dimensions) before flash-cooling by plunging into liquid nitrogen. X-ray data were recorded on beamline I04-1 at the Diamond Light Source

bioRxiv preprint doi: https://doi.org/10.1101/816959; this version posted May 5, 2021. The copyright holder for this preprint (which was not certified by peer review) is the author/funder, who has granted bioRxiv a license to display the preprint in perpetuity. It is made available under aCC-BY 4.0 International license.

(Oxfordshire, UK) using a Pilatus 6M-F hybrid photon counting detector (Dectris), with crystals maintained at 100 K by a Cryojet cryocooler (Oxford Instruments). Diffraction data were integrated and scaled using XDS[35] via the XIA2 expert system[36] then merged using AIMLESS[37]. Data collection statistics are summarized in Table 1. The majority of the downstream analysis was performed through the CCP4i2 graphical user interface[38].

The ParBΔCTD-*parS* complex crystallized in space group $P2_1$ with cell parameters of a = 54.3, b = 172.9, c = 72.9 Å and β = 90.5° (Table 1). Analysis of the likely composition of the asymmetric unit (ASU) suggested that it contains four copies of the ParBΔCTD monomer and two copies of the 22-bp *parS* DNA duplex, giving an estimated solvent content of ~47%.

Interrogation of the Protein Data Bank with the sequence of the *C. crescentus* ParBΔCTD revealed two suitable template structures for molecular replacement: apo-ParBΔCTD from *Thermus thermophilus*[39] (PDB accession code: 1VZ0; 46% identity over 82% of the sequence) and *Helicobacter pylori* ParBΔCTD bound to *parS* DNA[29] (PDB accession code: 4UMK; 42% identity over 75% of the sequence). First, single subunits taken from these two entries were trimmed using SCULPTOR[40] to retain the parts of the structure that aligned with the *C. crescentus* ParBΔCTD sequence, and then all side chains were truncated to Cβ atoms using CHAINSAW[41]. Comparison of these templates revealed a completely different relationship between the N-terminal domain and the DNA-binding domain. Thus, we prepared search templates based on the individual domains rather than the subunits. The pairs of templates for each domain were then aligned and used as ensemble search models in PHASER[42]. For the DNA component, an ideal B-form DNA duplex was generated in COOT[43] from a 22-bp palindromic sequence of *parS*. A variety of protocols were attempted in PHASER[42], the best result was obtained by searching for the two DNA duplexes first, followed by four copies of the DNA-binding domain, giving a TFZ score of 10.5 at 4.5 Å resolution. We found that the placement of the DNA-binding domains with respect to the DNA duplexes was analogous to that seen in the *H. pylori* ParBΔCTD-*parS* complex. After several iterations of rebuilding in COOT and refining the model in REFMAC5[44], it was possible to manually dock one copy of the N-terminal domain template (from 1VZ0) into weak and fragmented electron density such that it could be joined to one of the DNA-binding domains. A superposition of this more complete subunit onto the other three copies revealed that in only one of these did the N-terminal domain agree with the electron density. Inspection of the remaining unfilled electron density showed evidence for the last two missing N-terminal domains, which were also added by manual docking of the domain template (from 1VZ0). For the final stages, TLS refinement was used with a single TLS domain defined for each protein chain and for each DNA strand. The statistics of the final refined model, including validation output from MolProbity[45], are summarized in Table 1.

Crystallization screens for the *C. crescentus* ParBΔCTD-CTPγS complex crystal were also set up in sitting-drop vapour diffusion format in MRC2 96-well crystallization plates with drops comprised of 0.3 µL precipitant solution and 0.3 µL of protein solution (approx. 10 mg/mL) supplemented with 1 mM CTPγS (Jena Biosciences) and 1 mM $MgCl_2$, and incubated at 293 K. The ParBΔCTD-CTPγS crystals grew in a solution containing 15% (w/v) PEG 3350, 0.26 M calcium acetate, 10% (v/v) glycerol, 1 mM CTPγS, and 1 mM $MgCl_2$. Suitable crystals were cryoprotected with 20% (v/v) glycerol and mounted in Litholoops (Molecular Dimensions) before flash-cooling by plunging into liquid nitrogen. X-ray data were recorded on beamline I03 at the Diamond Light Source (Oxfordshire, UK) using an Eiger2 XE 16M hybrid photon counting detector (Dectris), with crystals maintained at 100 K by a Cryojet cryocooler (Oxford Instruments). Diffraction data were integrated and scaled using DIALS[46] via the XIA2 expert system[36] then merged using AIMLESS[37]. Data collection statistics are summarized in Table 1. The majority of the downstream analysis was performed through the CCP4i2 graphical user interface[38].

The ParBΔCTD-CTPγS complex crystallized in space group $P2_1$ with cell parameters of a = 69.5, b = 56.1, c = 71.4 Å and β = 98.4° (Table 1). Analysis of the likely composition of the asymmetric unit (ASU) suggested that it contains two copies of the ParBΔCTD monomer giving an estimated solvent content of ~50%. Molecular replacement templates were generated from the ParBΔCTD-*parS*

bioRxiv preprint doi: https://doi.org/10.1101/816959; this version posted May 5, 2021. The copyright holder for this preprint (which was not certified by peer review) is the author/funder, who has granted bioRxiv a license to display the preprint in perpetuity. It is made available under aCC-BY 4.0 International license.

complex solved above. Attempts to solve the structure in PHASER using individual subunits taken from the latter in both conformations did not yield any convincing solutions, suggesting that the subunits had adopted new conformations. Given that the two subunit conformations observed in the previous structure differed largely in the relative dispositions of DBD and NTDs, we reasoned that a better outcome might be achieved by searching for the DNA-binding domains and N-terminal domains separately. This time PHASER successfully placed two copies of each domain in the ASU such that they could be reconnected to give two subunits in a new conformation. The result was subjected to 100 cycles of jelly-body refinement in REFMAC5 before rebuilding with BUCCANEER[47] to give a model in which 77% of the expected residues had been fitted into two chains and sequenced. The model was completed after further iterations of model editing in COOT and refinement with REFMAC5. In this case, TLS refinement was not used as this gave poorer validation results. The statistics of the final refined model, including validation output from MolProbity[45], are summarized in Table 1.

Measurement of protein-DNA interaction by bio-layer interferometry (BLI) assay

Bio-layer interferometry experiments were conducted using a BLItz system equipped with High Precision Streptavidin 2.0 (SAX2) Biosensors (Molecular Devices). BLItz monitors wavelength shifts (nm) resulting from changes in the optical thickness of the sensor surface during association or dissociation of the analyte. All BLI experiments were performed at 22°C. The streptavidin biosensor was hydrated in a low-salt binding buffer [100 mM Tris-HCl pH 8.0, 100 mM NaCl, 1 mM $MgCl_2$, and 0.005% (v/v) Tween 20] for at least 10 minutes before each experiment. Biotinylated double-stranded DNA (dsDNA) was immobilized onto the surface of the SA biosensor through a cycle of Baseline (30 sec), Association (120 sec), and Dissociation (120 sec). Briefly, the tip of the biosensor was dipped into a binding buffer for 30 sec to establish the baseline, then to 1 μM biotinylated dsDNA for 120 sec, and finally to a low salt binding buffer for 120 sec to allow for dissociation.

After the immobilization of DNA on the sensor, association reactions were monitored at 1 μM dimer concentration of ParB with an increasing concentration of CTP (0, 1, 5, 10, 50, 100, 500, 1000 μM) for 120 sec. At the end of each binding step, the sensor was transferred into a protein-free binding buffer to follow the dissociation kinetics for 120 sec. The sensor can be recycled by dipping in a high-salt buffer [100 mM Tris-HCl pH 8.0, 1000 mM NaCl, 10 mM EDTA, and 0.005% (v/v) Tween 20] for 5 minutes to remove bound ParB.

For the dissociation step in the BLI experiments in Figure 7A, the probe was returned to either a low-salt binding buffer [100 mM Tris-HCl pH 8.0, 100 mM NaCl, 1 mM $MgCl_2$, and 0.005% (v/v) Tween 20] for 30 sec or a high-salt buffer [100 mM Tris-HCl pH 8.0, 1 M NaCl, 1 mM $MgCl_2$, and 0.005% (v/v) Tween 20] for 30 sec.

For experiments in Figure 7C, DNA-coated tips were dipped into 300 μL of restriction solution [266 μL of water, 30 μL of 10x buffer 3.1 (NEB), and 3 μL of BamHI restriction enzyme (20,000 units/mL)] for 2 hours at 37°C. As a result, closed DNA on the BLI surface was cleaved to generate a free DNA end.

All sensorgrams recorded during BLI experiments were analyzed using the BLItz analysis software (BLItz Pro version 1.2, Molecular Devices) and replotted in R for presentation. Each experiment was triplicated, standard deviations were calculated in Excel, and a representative sensorgram was presented in Figure 6-figure supplement 2B and Figure 7.

Differential radical capillary action of ligand assay (DRaCALA) or membrane-spotting assay

Purified *C. crescentus* ParB-His_6 (WT and mutants, at final concentrations of 0.7, 1.5, 3.1, 6.2, and 12.5 μM) were incubated with 5 nM radiolabeled P^{32}-α-CTP (Perkin Elmer), 30 μM of unlabeled CTP (ThermoFisher), and 1.5 μM of 22-bp *parS* DNA duplex in the binding buffer [100 mM Tris pH 8.0, 100 mM NaCl, and 10 mM $CaCl_2$] for 5 minutes at room temperature. Four μL of samples were spotted slowly onto a nitrocellulose membrane and air-dried. The nitrocellulose membrane was wrapped in cling film before being exposed to a phosphor screen (GE Healthcare) for two minutes. Each DRaCALA assay was triplicated, and a representative autoradiograph was shown. Data were quantified using Multi-Gauge

bioRxiv preprint doi: https://doi.org/10.1101/816959; this version posted May 5, 2021. The copyright holder for this preprint (which was not certified by peer review) is the author/funder, who has granted bioRxiv a license to display the preprint in perpetuity. It is made available under aCC-BY 4.0 International license.

software 3.0 (Fujifilm), the bound fraction were quantified as described previously[48]. Error bars represent standard deviations from triplicated experiments.

Measurement of CTPase activity by EnzCheck phosphate release assay

CTP hydrolysis was monitored using an EnzCheck Phosphate Assay Kit (ThermoFisher). Samples (100 µL) containing a reaction buffer supplemented with an increasing concentration of CTP (0, 1, 5, 10, 50, 100, 500, and 1000 µM), 0.5 µM of 22-bp *parS* DNA, and 1 µM ParB (WT or mutants) were assayed in a Biotek EON plate reader at 25°C for 8 hours with readings every minute. The reaction buffer (1 mL) typically contained: 740 µL Ultrapure water, 50 µL 20x reaction buffer [100 mM Tris pH 8.0, 2 M NaCl, and 20 mM $MgCl_2$], 200 µL MESG substrate solution, and 10 µL purine nucleoside phosphorylase enzyme (1 unit). Reactions with buffer only or buffer + CTP + 22-bp *parS* DNA only were also included as controls. The plates were shaken at 280 rpm continuously for 8 hours at 25°C. The inorganic phosphate standard curve was also constructed according to the manual. The results were analyzed using Excel and the CTPase rates were calculated using a linear regression fitting in Excel. Error bars represent standard deviations from triplicated experiments.

***In vitro* crosslinking assay using a sulfhydryl-to-sulfhydryl crosslinker bismaleimidoethane (BMOE)**

A 50 µL mixture of 8 µM ParB mutants (with residues at specific positions in the NTD, DBD, or CTD substituted to cysteine) ± CTP (0 to 1000 µM) ± 0.5 µM DNA (a 22-bp linear DNA or a 3-kb circular *parS*/scrambled *parS* plasmid) was assembled in a reaction buffer [10 mM Tris-HCl pH 7.4, 100 mM NaCl, and 1 mM $MgCl_2$] and incubated for 5 minutes at room temperature. BMOE (1 mM final concentration from a 20 mM stock solution) was then added, and the reaction was quickly mixed by three pulses of vortexing. SDS-PAGE sample buffer containing 23 mM β-mercaptoethanol was then added immediately to quench the crosslinking reaction. Samples were heated to 50°C for 5 minutes before being loaded on 12% Novex WedgeWell Tris-Glycine gels (ThermoFisher). Protein bands were stained with an InstantBlue Coomassie solution (Abcam) and band intensity was quantified using Image Studio Lite version 5.2 (LI-COR Biosciences). The crosslinked fractions were averaged, and their standard deviations from triplicated experiments were calculated in Excel.

For the experiment described in Lane 8 of Figure 5C-D and Figure 5-figure supplement 1, crosslinking reactions were performed as described above, however the reaction were quenched using a quenching buffer [10 mM Tris-HCl pH 7.4, 100 mM NaCl, 1 mM $MgCl_2$, and 2.3 mM β-mercaptoethanol] instead. Subsequently, 1 µL of a non-specific DNA nuclease (Benzonase, 250 units/ µL, Merck) was added, the mixture was incubated at room temperature for a further 10 minutes before SDS-PAGE sample buffer was added. Samples were heated to 50°C for 5 minutes before being loaded on 4-12% Novex WedgeWell Tris-Glycine gels (ThermoFisher).

For the experiments described in Lane 8 of Figure 5-figure supplement 2A, crosslinking and quenching reactions were performed as described above before 1 µL of TEV protease (10 units/µL, ThermoFisher) was added. The mixture was incubated at room temperature for a further 30 minutes before SDS-PAGE sample buffer was added. Samples were heated to 50°C for 5 minutes before being loaded on 4-12% Novex WedgeWell Tris-Glycine gels.

For experiments described in Lane 9 of Figure 5-figure supplement 2B, proteins were released from gel slices by a “crush & soak” method. Briefly, ten gel slices were cut out from unstained SDS-PAGE gels and transferred to a 2-mL Eppendorf tube. Gel slices were frozen in liquid nitrogen and were crushed using a plastic pestle. The resulting paste was soaked in 500 µL of soaking buffer [10 mM Tris-HCl pH 8, 100 mM NaCl, 1 mM $MgCl_2$, and1 µL of Benzonase (250 units/µL)], and the tube was incubated with rotation in a rotating wheel overnight. On the next day, the tube was centrifuged at 13,000 rpm for 5 minutes and the supernatant was transferred to a new 1.5 mL Eppendorf tube. The sample volume was reduced to approx. 50 µL using a SpeedVac vacuum concentrator before SDS-PAGE sample buffer was added in. The entire sample was loaded onto a single well of a 4-12% WedgeWell Tris-Glycine gel.

bioRxiv preprint doi: https://doi.org/10.1101/816959; this version posted May 5, 2021. The copyright holder for this preprint (which was not certified by peer review) is the author/funder, who has granted bioRxiv a license to display the preprint in perpetuity. It is made available under aCC-BY 4.0 International license.

Gels were submerged in an InstantBlue Coomassie solution (Abcam) to stain for protein, or in a SYBR Green solution (ThermoFisher) to stain for DNA. Denatured samples were also loaded on 1% TAE agarose gels and electrophoresed at 120V for 40 minutes at room temperature. Afterwards, agarose gels were submerged in a SYBR green solution to stain for DNA.

Chromatin immunoprecipitation with deep sequencing (ChIP-seq)

ChIP-seq experiments and subsequent data analysis were performed exactly as reported previously[11]. Each ChIP-seq experiment was duplicated using biological replicates. For the list of ChIP-seq experiments and their replicates in this study, see Supplementary File S2.

Immunoblot analysis

For Western blot analysis, *C. crescentus* cells were pelleted and resuspended directly in 1xSDS sample buffer, then heated to 95°C for 5 min before loading. Total protein was run on 12% Novex WedgeWell gels (ThermoFisher) at 150 V for separation. Resolved proteins were transferred to PVDF membranes using the Trans-Blot Turbo Transfer System (BioRad) and probed with 1:10,000 dilution of α-FLAG HRP-conjugated antibodies (Sigma-Aldrich) antibody. Blots were imaged using an Amersham Imager 600 (GE Healthcare).

bioRxiv preprint doi: https://doi.org/10.1101/816959; this version posted May 5, 2021. The copyright holder for this preprint (which was not certified by peer review) is the author/funder, who has granted bioRxiv a license to display the preprint in perpetuity. It is made available under aCC-BY 4.0 International license.

TABLE 1. X-ray data collection and processing statistics

Structure	***C. crescentus* ParBΔCTD-*parS* complex**	***C. crescentus* ParBΔCTD CTPγS complex**
Data collection		
Diamond Light Source beamline	I04-1	I03
Wavelength (Å)	0.916	0.976
Detector	Pilatus 6M-F	Eiger2 XE 16M
Resolution range (Å)	72.96 – 2.90 (3.08 – 2.90)	70.59 – 2.73 (2.86 – 2.73)
Space Group	$P2_1$	$P2_1$
Cell parameters (Å/°)	a = 54.3, b = 172.9, c = 72.9, β = 90.5	a = 69.5, b = 56.1, c = 71.4, β = 98.4
Total no. of measured intensities	198135 (33888)	92266 (8473)
Unique reflections	29654 (4775)	14516 (1756)
Multiplicity	6.7 (7.1)	6.4 (4.8)
Mean $I/\sigma(I)$	8.7 (1.4)	5.4 (1.2)
Completeness (%)	99.7 (100.0)	98.8 (91.4)
R_{merge}[a]	0.135 (1.526)	0.195 (1.210)
R_{meas}[b]	0.146 (1.646)	0.212 (1.357)
$CC_{½}$[c]	0.997 (0.677)	0.991 (0.825)
Wilson B value (Å^2)	81.6	57.7
Refinement		
Resolution range (Å)	72.96 – 2.90 (2.98 – 2.90)	70.59 – 2.73 (2.80 – 2.73)
Reflections: working/free[d]	28155/1466	13824/678
R_{work}[e]	0.240 (0.366)	0.248 (0.371)
R_{free}[e]	0.263 (0.369)	0.284 (0.405)
Ramachandran plot: favored/allowed/disallowed[f] (%)	95.2/4.8/0	95.5/4.5/0
R.m.s. bond distance deviation (Å)	0.005	0.002
R.m.s. bond angle deviation (°)	1.05	1.19
Mean B factors: protein/DNA/other/ overall (Å^2)	98/74/-/92	81/-/61/77
PDB accession code	**6T1F**	**7BM8**

Values in parentheses are for the outer resolution shell.

[a] $R_{merge} = \sum_{hkl} \sum_i |I_i(hkl) - \langle I(hkl)\rangle| / \sum_{hkl} \sum_i I_i(hkl)$.

bioRxiv preprint doi: https://doi.org/10.1101/816959; this version posted May 5, 2021. The copyright holder for this preprint (which was not certified by peer review) is the author/funder, who has granted bioRxiv a license to display the preprint in perpetuity. It is made available under aCC-BY 4.0 International license.

[b] $R_{meas} = \sum_{hkl} [N/(N-1)]^{1/2} \times \sum_i |I_i(hkl) - \langle I(hkl)\rangle| / \sum_{hkl} \sum_i I_i(hkl)$, where $I_i(hkl)$ is the ith observation of reflection hkl, $\langle I(hkl)\rangle$ is the weighted average intensity for all observations i of reflection hkl and N is the number of observations of reflection hkl.

[c] $CC_{½}$ is the correlation coefficient between symmetry equivalent intensities from random halves of the dataset.

[d] The dataset was split into "working" and "free" sets consisting of 95 and 5% of the data respectively. The free set was not used for refinement.

[e] The R-factors R_{work} and R_{free} are calculated as follows: $R = \sum(|F_{obs} - F_{calc}|)/\sum|F_{obs}|$, where F_{obs} and F_{calc} are the observed and calculated structure factor amplitudes, respectively.

[f] As calculated using MolProbity [45].

bioRxiv preprint doi: https://doi.org/10.1101/816959; this version posted May 5, 2021. The copyright holder for this preprint (which was not certified by peer review) is the author/funder, who has granted bioRxiv a license to display the preprint in perpetuity. It is made available under aCC-BY 4.0 International license.

REFERENCES

1. Jalal, A. S. & Le, T. B. Bacterial chromosome segregation by the ParABS system. *Open Biology* **10**, 200097 (2020).
2. Donczew, M. *et al.* ParA and ParB coordinate chromosome segregation with cell elongation and division during Streptomyces sporulation. *Open Biology* **6**, 150263 (2016).
3. Fogel, M. A. & Waldor, M. K. A dynamic, mitotic-like mechanism for bacterial chromosome segregation. *Genes Dev.* **20**, 3269–3282 (2006).
4. Harms, A., Treuner-Lange, A., Schumacher, D. & Sogaard-Andersen, L. Tracking of chromosome and replisome dynamics in Myxococcus xanthus reveals a novel chromosome arrangement. *PLoS Genet* **9**, e1003802 (2013).
5. Ireton, K., Gunther, N. W. & Grossman, A. D. spo0J is required for normal chromosome segregation as well as the initiation of sporulation in Bacillus subtilis. *Journal of Bacteriology* **176**, 5320–5329 (1994).
6. Jakimowicz, D., Chater, K. & Zakrzewska-Czerwi´nska, J. The ParB protein of Streptomyces coelicolor A3(2) recognizes a cluster of parS sequences within the origin-proximal region of the linear chromosome. *Molecular Microbiology* **45**, 1365–1377 (2002).
7. Kawalek, A., Bartosik, A. A., Glabski, K. & Jagura-Burdzy, G. Pseudomonas aeruginosa partitioning protein ParB acts as a nucleoid-associated protein binding to multiple copies of a parS-related motif. *Nucleic Acids Res.* **46**, 4592–4606 (2018).
8. Lin, D. C.-H. & Grossman, A. D. Identification and Characterization of a Bacterial Chromosome Partitioning Site. *Cell* **92**, 675–685 (1998).
9. Livny, J., Yamaichi, Y. & Waldor, M. K. Distribution of Centromere-Like parS Sites in Bacteria: Insights from Comparative Genomics. *J. Bacteriol.* **189**, 8693–8703 (2007).
10. Mohl, D. A., Easter, J. & Gober, J. W. The chromosome partitioning protein, ParB, is required for cytokinesis in Caulobacter crescentus. *Mol. Microbiol.* **42**, 741–755 (2001).
11. Tran, N. T. *et al.* Permissive zones for the centromere-binding protein ParB on the Caulobacter crescentus chromosome. *Nucleic Acids Res* **46**, 1196–1209 (2018).
12. Breier, A. M. & Grossman, A. D. Whole-genome analysis of the chromosome partitioning and sporulation protein Spo0J (ParB) reveals spreading and origin-distal sites on the Bacillus subtilis chromosome. *Molecular Microbiology* **64**, 703–718 (2007).
13. Taylor, J. A. *et al.* Specific and non-specific interactions of ParB with DNA: implications for chromosome segregation. *Nucleic Acids Res* **43**, 719–731 (2015).
14. Graham, T. G. W. *et al.* ParB spreading requires DNA bridging. *Genes Dev.* **28**, 1228–1238 (2014).
15. Sanchez, A. *et al.* Stochastic Self-Assembly of ParB Proteins Builds the Bacterial DNA Segregation Apparatus. *Cell Syst.* **1**, 163–173 (2015).
16. Broedersz, C. P. *et al.* Condensation and localization of the partitioning protein ParB on the bacterial chromosome. *PNAS* **111**, 8809–8814 (2014).
17. Murray, H., Ferreira, H. & Errington, J. The bacterial chromosome segregation protein Spo0J spreads along DNA from parS nucleation sites. *Molecular Microbiology* **61**, 1352–1361 (2006).
18. Lim, H. C. *et al.* Evidence for a DNA-relay mechanism in ParABS-mediated chromosome segregation. *Elife* **3**, e02758 (2014).
19. Vecchiarelli, A. G., Mizuuchi, K. & Funnell, B. E. Surfing biological surfaces: exploiting the nucleoid for partition and transport in bacteria. *Molecular Microbiology* **86**, 513–523 (2012).
20. Vecchiarelli, A. G., Neuman, K. C. & Mizuuchi, K. A propagating ATPase gradient drives transport of surface-confined cellular cargo. *PNAS* **111**, 4880–4885 (2014).
21. Hwang, L. C. *et al.* ParA-mediated plasmid partition driven by protein pattern self-organization. *The EMBO Journal* **32**, 1238–1249 (2013).
22. Leonard, T. A., Butler, P. J. & Löwe, J. Bacterial chromosome segregation: structure and DNA binding of the Soj dimer--a conserved biological switch. *EMBO J.* **24**, 270–282 (2005).

bioRxiv preprint doi: https://doi.org/10.1101/816959; this version posted May 5, 2021. The copyright holder for this preprint (which was not certified by peer review) is the author/funder, who has granted bioRxiv a license to display the preprint in perpetuity. It is made available under aCC-BY 4.0 International license.

23. Taylor, J. A., Seol, Y., Neuman, K. C. & Mizuuchi, K. CTP and parS control ParB partition complex dynamics and ParA-ATPase activation for ParABS-mediated DNA partitioning. *bioRxiv* 2021.01.24.427996 (2021) doi:10.1101/2021.01.24.427996.
24. Jalal, A. S., Tran, N. T. & Le, T. B. ParB spreading on DNA requires cytidine triphosphate in vitro. *eLife* **9**, e53515 (2020).
25. Osorio-Valeriano, M. *et al.* ParB-type DNA Segregation Proteins Are CTP-Dependent Molecular Switches. *Cell* **179**, 1512-1524.e15 (2019).
26. Soh, Y.-M. *et al.* Self-organization of parS centromeres by the ParB CTP hydrolase. *Science* **366**, 1129–1133 (2019).
27. Figge, R. M., Easter, J. & Gober, J. W. Productive interaction between the chromosome partitioning proteins, ParA and ParB, is required for the progression of the cell cycle in Caulobacter crescentus. *Mol. Microbiol.* **47**, 1225–1237 (2003).
28. Jalal, A. S. B. *et al.* Diversification of DNA-Binding Specificity by Permissive and Specificity-Switching Mutations in the ParB/Noc Protein Family. *Cell Rep* **32**, 107928 (2020).
29. Chen, B.-W., Lin, M.-H., Chu, C.-H., Hsu, C.-E. & Sun, Y.-J. Insights into ParB spreading from the complex structure of Spo0J and parS. *Proc. Natl. Acad. Sci. U.S.A.* **112**, 6613–6618 (2015).
30. Krissinel, E. Stock-based detection of protein oligomeric states in jsPISA. *Nucleic Acids Res.* **43**, W314-319 (2015).
31. Fisher, G. L. *et al.* The structural basis for dynamic DNA binding and bridging interactions which condense the bacterial centromere. *Elife* **6**, (2017).
32. De March, M. *et al.* Structural basis of human PCNA sliding on DNA. *Nature Communications* **8**, 13935 (2017).
33. Thanbichler, M., Iniesta, A. A. & Shapiro, L. A comprehensive set of plasmids for vanillate- and xylose-inducible gene expression in Caulobacter crescentus. *Nucl. Acids Res.* **35**, e137–e137 (2007).
34. Thanbichler, M. & Shapiro, L. MipZ, a Spatial Regulator Coordinating Chromosome Segregation with Cell Division in Caulobacter. *Cell* **126**, 147–162 (2006).
35. Kabsch, W. XDS. *Acta Crystallogr D Biol Crystallogr* **66**, 125–132 (2010).
36. Winter, G. xia2: an expert system for macromolecular crystallography data reduction. *J Appl Cryst* **43**, 186–190 (2010).
37. Evans, P. R. & Murshudov, G. N. How good are my data and what is the resolution? *Acta Cryst D* **69**, 1204–1214 (2013).
38. Potterton, L. *et al.* CCP4i2: the new graphical user interface to the CCP4 program suite. *Acta Crystallogr D Struct Biol* **74**, 68–84 (2018).
39. Leonard, T. A., Butler, P. J. G. & Löwe, J. Structural analysis of the chromosome segregation protein Spo0J from Thermus thermophilus. *Mol. Microbiol.* **53**, 419–432 (2004).
40. Bunkóczi, G. & Read, R. J. Improvement of molecular-replacement models with Sculptor. *Acta Crystallogr D Biol Crystallogr* **67**, 303–312 (2011).
41. Stein, N. CHAINSAW: a program for mutating pdb files used as templates in molecular replacement. *J Appl Cryst* **41**, 641–643 (2008).
42. McCoy, A. J. *et al.* Phaser crystallographic software. *J Appl Crystallogr* **40**, 658–674 (2007).
43. Emsley, P. & Cowtan, K. Coot: model-building tools for molecular graphics. *Acta Crystallogr. D Biol. Crystallogr.* **60**, 2126–2132 (2004).
44. Murshudov, G. N., Vagin, A. A. & Dodson, E. J. Refinement of Macromolecular Structures by the Maximum-Likelihood Method. *Acta Cryst D* **53**, 240–255 (1997).
45. Chen, V. B. *et al.* MolProbity: all-atom structure validation for macromolecular crystallography. *Acta Crystallogr. D Biol. Crystallogr.* **66**, 12–21 (2010).
46. Winter, G. *et al.* DIALS: implementation and evaluation of a new integration package. *Acta Crystallogr D Struct Biol* **74**, 85–97 (2018).

bioRxiv preprint doi: https://doi.org/10.1101/816959; this version posted May 5, 2021. The copyright holder for this preprint (which was not certified by peer review) is the author/funder, who has granted bioRxiv a license to display the preprint in perpetuity. It is made available under aCC-BY 4.0 International license.

47. Cowtan, K. The Buccaneer software for automated model building. 1. Tracing protein chains. *Acta Crystallogr. D Biol. Crystallogr.* **62**, 1002–1011 (2006).
48. Roelofs, K. G., Wang, J., Sintim, H. O. & Lee, V. T. Differential radial capillary action of ligand assay for high-throughput detection of protein-metabolite interactions. *Proc Natl Acad Sci U S A* **108**, 15528–15533 (2011).

bioRxiv preprint doi: https://doi.org/10.1101/816959; this version posted May 5, 2021. The copyright holder for this preprint (which was not certified by peer review) is the author/funder, who has granted bioRxiv a license to display the preprint in perpetuity. It is made available under aCC-BY 4.0 International license.

FIGURE 1

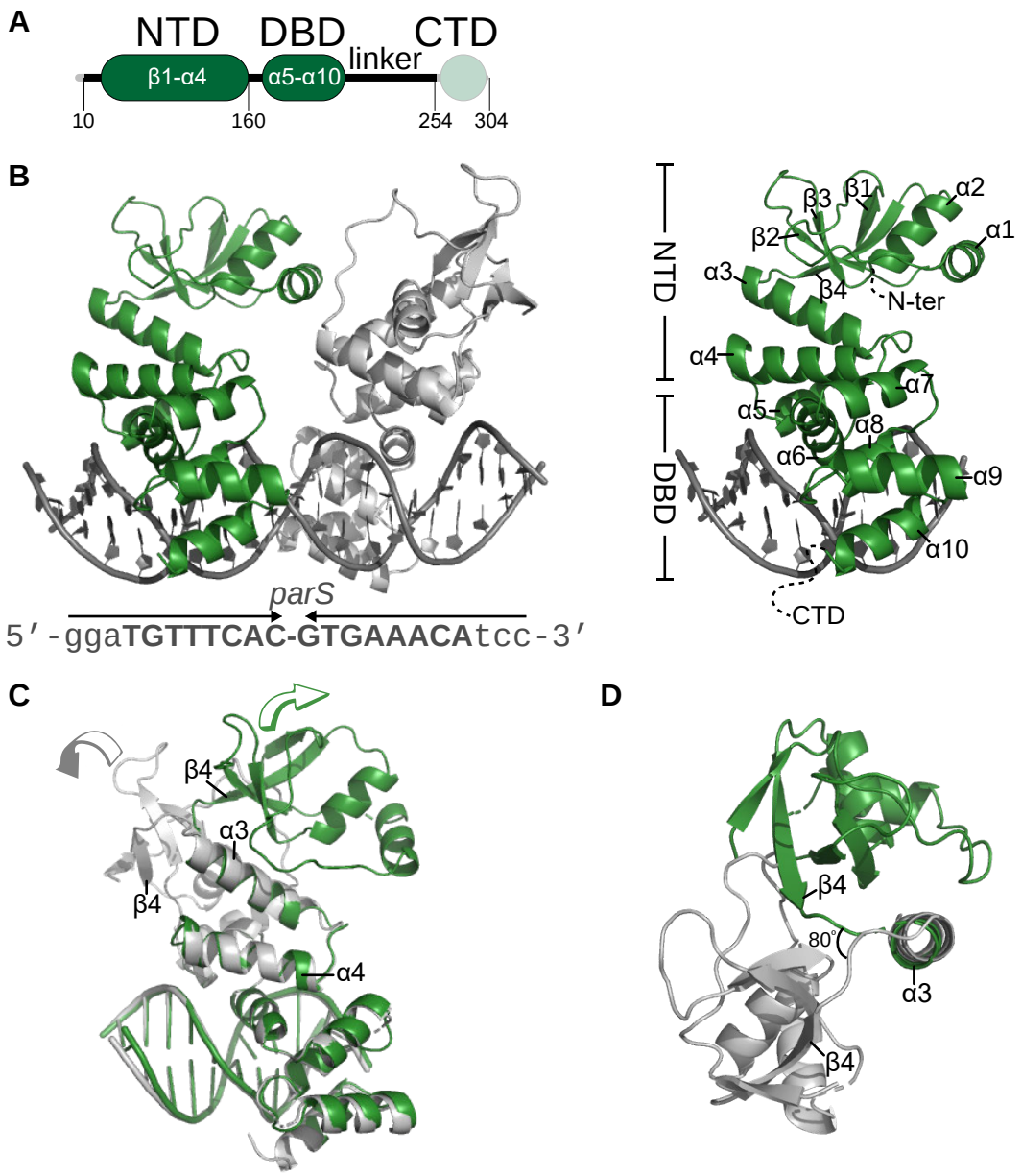

Figure 1. Co-crystal structure of a *C. crescentus* ParBΔCTD-*parS* complex reveals an open conformation at the NTD. (A) The domain architecture of *C. crescentus* ParB: the N-terminal domain (NTD, dark green), the central DNA-binding domain (DBD, dark green), the C-terminal domain (CTD, faded green), and a linker that connects the DBD and the CTD together. The ParBΔCTD variant that was used for crystallization lacks the CTD (faded green). **(B) (Left panel)** Co-crystal structure of two *C. crescentus* ParBΔCTD monomers (dark green and grey) bound to a 22-bp *parS* DNA. The nucleotide sequence of the 22-bp *parS* is shown below the co-crystal structure, the core *parS* sequence is highlighted in bold, and each *parS* half-site was denoted by an arrow. **(Right panel)** The structure of a ParBΔCTD subunit bound to a *parS* half site with key features highlighted. **(C)** Superimposition of *C. crescentus* ParBΔCTD subunits shows two different orientations of the NTD. The arrow above each subunit shows the direction each NTD is projecting towards. **(D)** A top-down view of the superimposition of ParBΔCTD subunits shows their NTDs orienting ~80° apart from each other.

bioRxiv preprint doi: https://doi.org/10.1101/816959; this version posted May 5, 2021. The copyright holder for this preprint (which was not certified by peer review) is the author/funder, who has granted bioRxiv a license to display the preprint in perpetuity. It is made available under aCC-BY 4.0 International license.

FIGURE 2

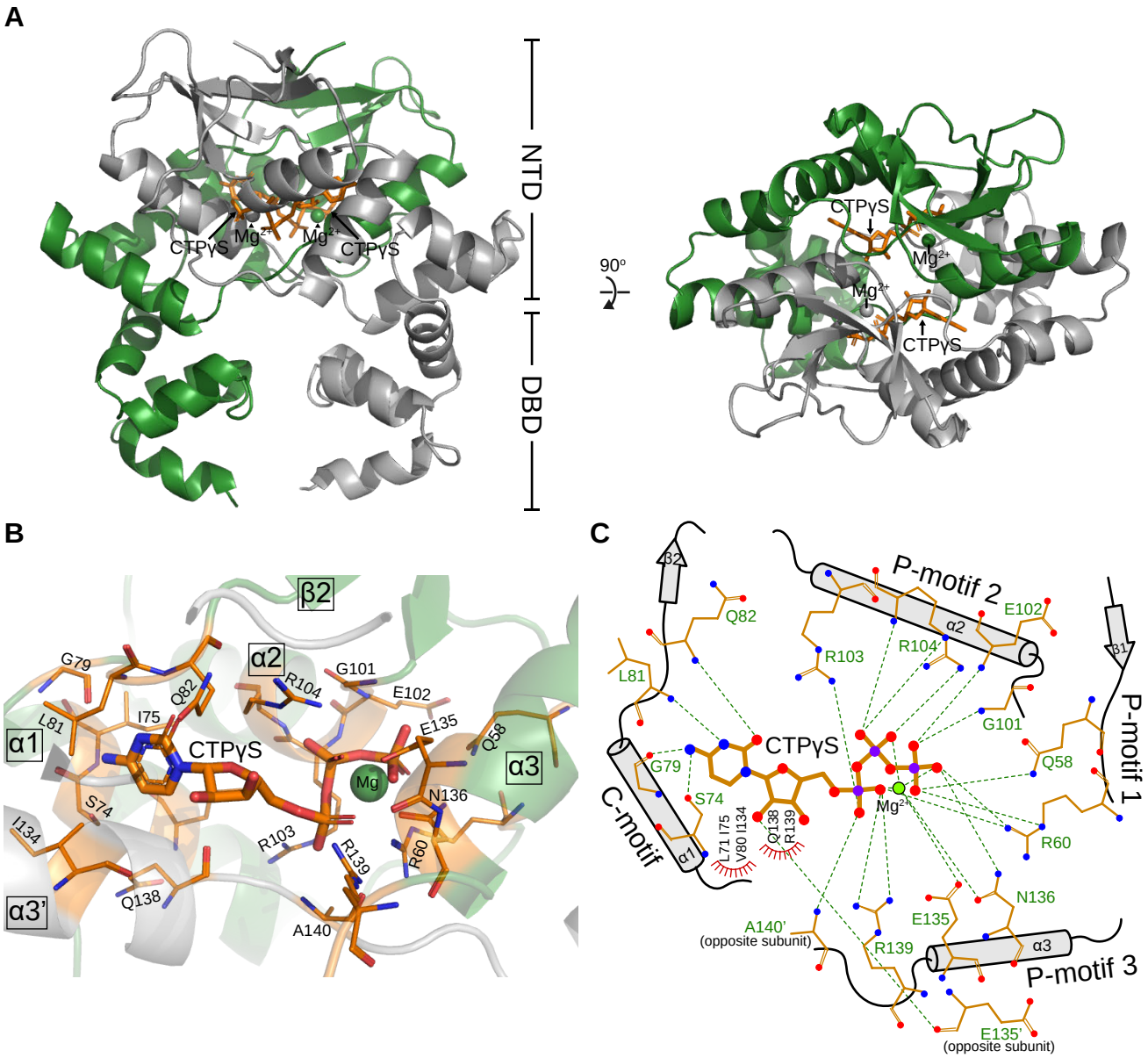

Figure 2. Co-crystal structure of a *C. crescentus* ParBΔCTD-CTPɣS complex reveals a closed conformation at the NTD. (A) (Left panel) The front view of the co-crystal structure of *C. crescentus* ParBΔCTD (dark green and grey) bound to a non-hydrolyzable analog CTPɣS (orange) and Mg^{2+} ions (dark green and grey spheres). **(Right panel)** The top view of the *C. crescentus* ParBΔCTD-CTPɣS co-crystal structure. **(B)** The nucleotide-binding pocket of *C. crescentus* ParB showing amino acid residues that contact the CTPɣS molecule and the coordinated Mg^{2+} ion. **(C)** Protein-ligand interaction map of CTPɣS bound to *C. crescentus* ParBΔCTD. Hydrogen bonds are shown as dashed green lines and hydrophobic interactions as red semi-circles. Nitrogen, oxygen, phosphate, and magnesium atoms are shown as blue, red, purple, and green filled circles, respectively.

bioRxiv preprint doi: https://doi.org/10.1101/816959; this version posted May 5, 2021. The copyright holder for this preprint (which was not certified by peer review) is the author/funder, who has granted bioRxiv a license to display the preprint in perpetuity. It is made available under aCC-BY 4.0 International license.

FIGURE 3

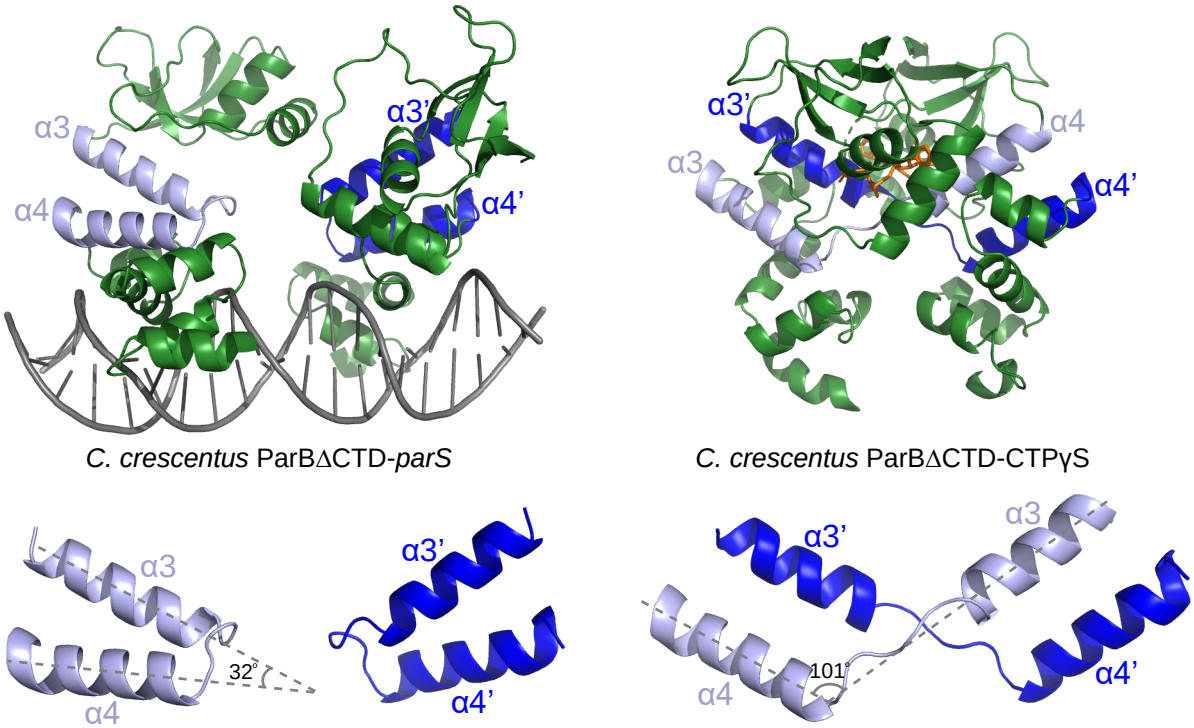

Figure 3. Conformational changes between the nucleating and the spreading states of *C. crescentus* ParB. Structures of *C. crescentus* ParBΔCTD in complex with *parS* **(left panel)** and with CTPɣS **(right panel)**, with the pairs of helices (α3-α4, and α3'-α4' for the opposite subunit) shown in light blue and dark blue, respectively. Below each structure, only the α3-α4, α3'-α4' pairs, and the angles between these helices are shown.

bioRxiv preprint doi: https://doi.org/10.1101/816959; this version posted May 5, 2021. The copyright holder for this preprint (which was not certified by peer review) is the author/funder, who has granted bioRxiv a license to display the preprint in perpetuity. It is made available under aCC-BY 4.0 International license.

FIGURE 4

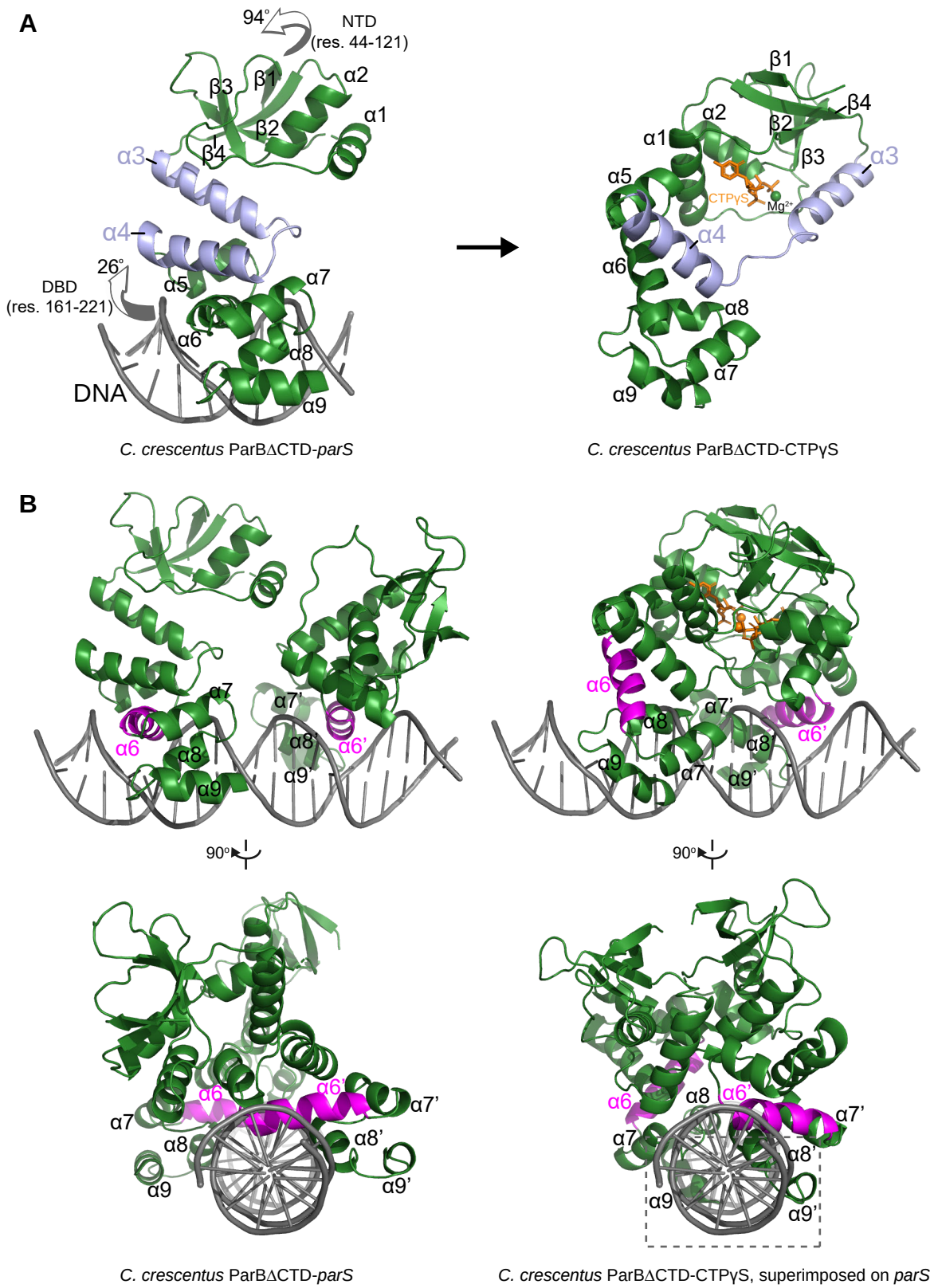

Figure 4. The structure of a nucleotide-bound *C. crescentus* ParBΔCTD is incompatible with specific *parS* binding at the DBD. (A) Structural changes between *C. crescentus* ParBΔCTD-*parS* and ParBΔCTD-CTPɣS structures. Helices α3 and α4 are shown in light blue. The arrows next to the NTD (residues 44 to 121) and the DBD (residues 161 to 221) show the direction that these domains rotate towards in the nucleotide-bound state. **(B)** Superimposing the *C. crescentus* ParBΔCTD-CTPɣS structure onto *parS* DNA shows DNA-recognition helices (α6 and α6', magenta) positioning away from the two consecutive major grooves of *parS*, and helices α8-α9 and α8'-α9' at the DBD (dashed box) clashing with *parS* DNA.

bioRxiv preprint doi: https://doi.org/10.1101/816959; this version posted May 5, 2021. The copyright holder for this preprint (which was not certified by peer review) is the author/funder, who has granted bioRxiv a license to display the preprint in perpetuity. It is made available under aCC-BY 4.0 International license.

FIGURE 5

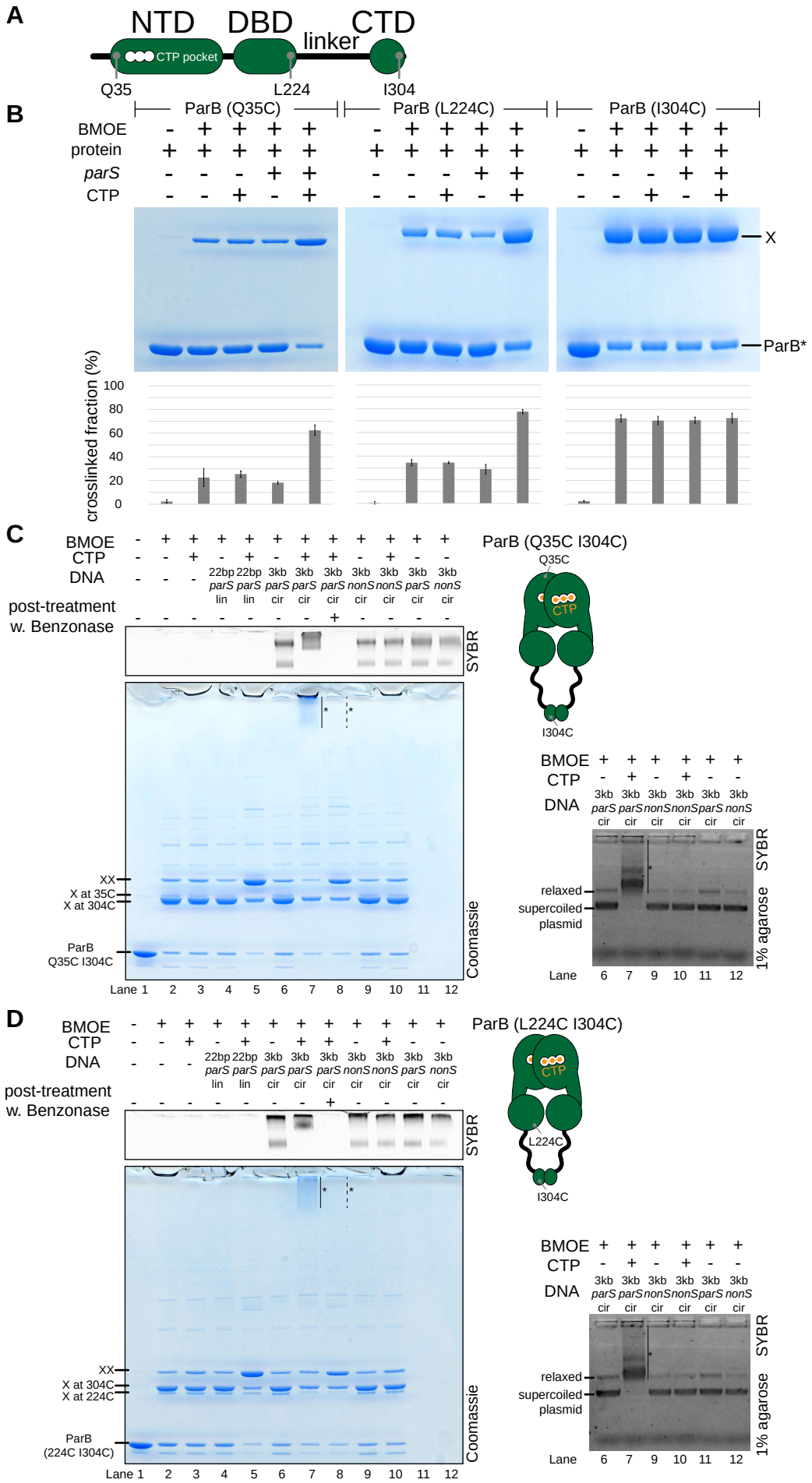

bioRxiv preprint doi: https://doi.org/10.1101/816959; this version posted May 5, 2021. The copyright holder for this preprint (which was not certified by peer review) is the author/funder, who has granted bioRxiv a license to display the preprint in perpetuity. It is made available under aCC-BY 4.0 International license.

Figure 5. *C. crescentus* ParB entraps *parS* DNA in a compartment between the DBD and the CTD in a CTP-dependent manner. (A) A schematic diagram of *C. crescentus* ParB showing the position of Q35 (at the NTD), L224 (at the DBD), and I304 (at the CTD) that were substituted either individually or in combinations for cysteine. **(B)** Denaturing polyacrylamide gel analysis of BMOE crosslinking products of 8 µM single-cysteine ParB (Q35C/L224C/I304C) variant ± 0.5 µM 22-bp *parS* DNA ± 1 mM CTP. X indicates a crosslinked form of ParB. Quantification of the crosslinked (X) fraction is shown below each representative gel image. Error bars represent SD from three replicates. **(C) (Left panel)** Denaturing polyacrylamide gel analysis of BMOE crosslinking products of 8 µM dual-cysteine ParB (Q35C I304C) variant ± 0.5 µM DNA ± 1 mM CTP. Different DNA were employed in crosslinking reactions: a linear 22-bp *parS* DNA (22 bp *parS* lin), a circular 3-kb *parS* plasmid (3 kb *parS* cir), and a circular 3-kb scrambled *parS* plasmid (3 kb *nonS* cir). The high molecular weight (HMW) smear near the top of the polyacrylamide gel is marked with a solid line and an asterisk (Lane 7). When the crosslinking reaction was post-treated with a non-specific DNA nuclease, Benzonase, the HMW smear was no longer observed (dashed line and asterisk, Lane 8). The polyacrylamide gel was also stained with a DNA-dye, Sybr Green (SYBR), and only the top section of the gel was shown. Small 22-bp *parS* DNA duplex migrated out of the gel, thus was not observed near the top of the Sybr-stained gel. A schematic diagram of a dual-cysteine *C. crescentus* ParB dimer is also shown. **(Right panel)** Agarose gel analysis of BMOE crosslinking products. A subset of crosslinking reactions (Lanes 6, 7, and 9-12) were loaded and resolved on 1% agarose gel. The gel was subsequently stained with Sybr Green for DNA. Shifted gel bands were marked with a solid line and an asterisk. **(D)** Same as panel **C** but another dual-cysteine variant, ParB (L224C I304C), was employed instead.

bioRxiv preprint doi: https://doi.org/10.1101/816959; this version posted May 5, 2021. The copyright holder for this preprint (which was not certified by peer review) is the author/funder, who has granted bioRxiv a license to display the preprint in perpetuity. It is made available under aCC-BY 4.0 International license.

FIGURE 6

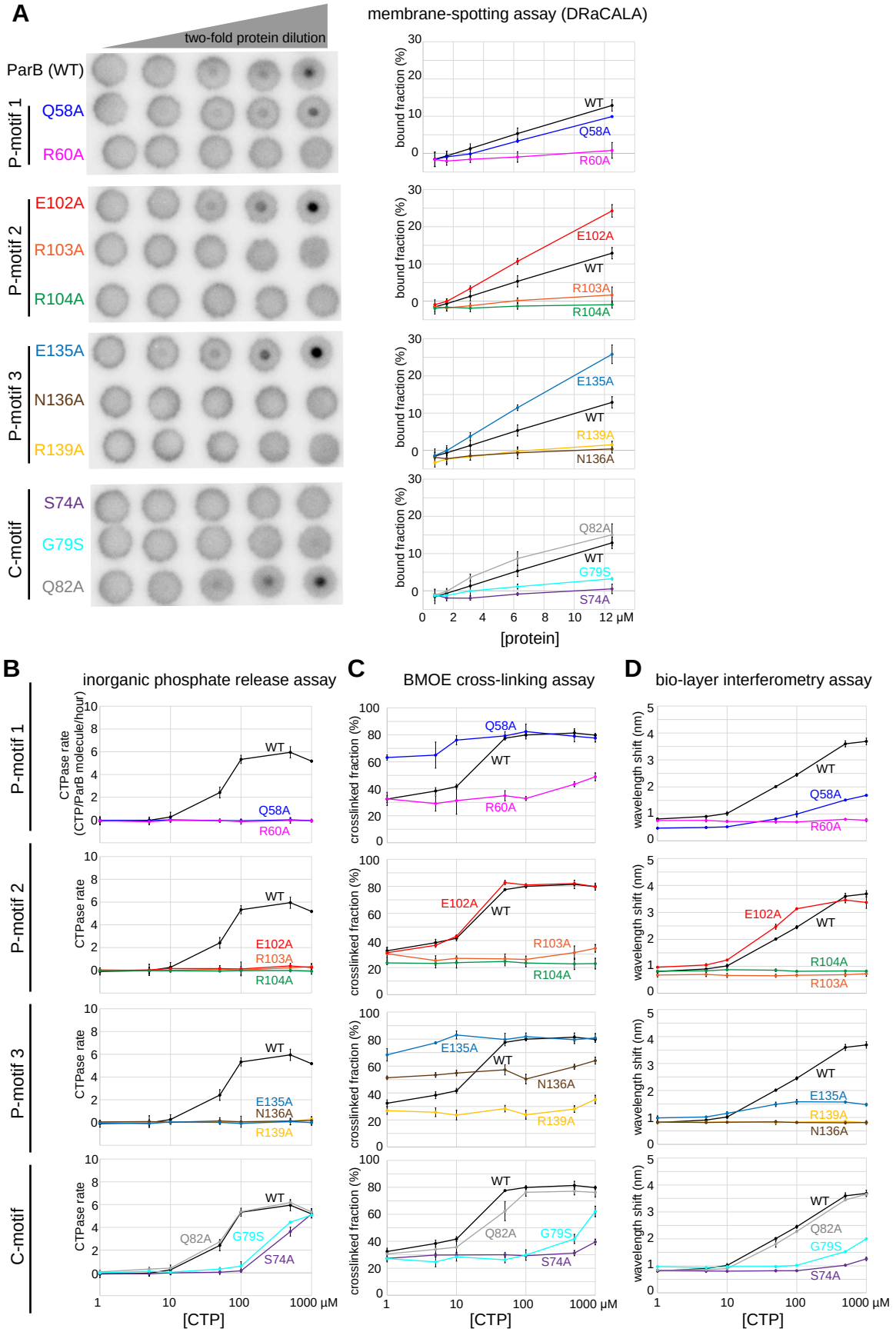

bioRxiv preprint doi: https://doi.org/10.1101/816959; this version posted May 5, 2021. The copyright holder for this preprint (which was not certified by peer review) is the author/funder, who has granted bioRxiv a license to display the preprint in perpetuity. It is made available under aCC-BY 4.0 International license.

Figure 6. Alanine scanning mutagenesis of the *C. crescentus* ParB CTP-binding pocket reveals several classes of clamp mutants. Eleven residues at C-motif and P-motifs 1 to 3 were individually substituted for alanine or glycine. **(A)** Membrane-spotting assay of ParB variants. CTP binding was monitored by membrane-spotting assay using radiolabeled CTP α-P^{32}. The bulls-eye staining indicates CTP binding due to a more rapid immobilization of protein-ligand complexes compared to free ligands. All reactions contained various concentration of purified ParB, 5 nM radiolabeled CTP α-P^{32}, 30 µM unlabeled CTP, and 1.5 µM 22-bp *parS* DNA. The bound fractions were quantified, and error bars represent SD from three replicates. All the reactions were spotted on the same membrane, the radiograph was rearranged solely for presentation purposes. **(B)** Inorganic phosphate release assay of ParB variants. The CTPase rates were measured at increasing concentration of CTP. All reactions contained 1 µM purified ParB variant, 0.5 µM 22-bp *parS* DNA, and an increasing concentration of CTP. **(C)** BMOE crosslinking assay of ParB variants. A second set of alanine scanning ParB variants, which harbor an additional Q35C substitution at the NTD, were also constructed and subsequently used in BMOE crosslinking experiments. Purified ParB variants (8 µM) were preincubated with 0.5 µM 22-bp *parS* DNA and an increasing concentration of CTP for 5 minutes before BMOE was added. Crosslinking products were resolved on a 12% denaturing polyacrylamide gel and the crosslinked fractions were quantified (see also Figure 6-figure supplement 1 for representation images). Error bars represent SD from three replicates. **(D)** Bio-layer interferometry (BLI) assay of ParB variants. BLI analysis of the interaction between a premix of 1 µM ParB variant ± an increasing concentration of CTP and a 170-bp closed *parS* DNA substrate. See also Figure 6-figure supplement 2A for a schematic diagram of the BLI setup, and Figure 6-figure supplement 2B for representative BLI sensorgrams. BLI signal at the end of the association phase (± SD from three replicates) was plotted against CTP concentrations.

bioRxiv preprint doi: https://doi.org/10.1101/816959; this version posted May 5, 2021. The copyright holder for this preprint (which was not certified by peer review) is the author/funder, who has granted bioRxiv a license to display the preprint in perpetuity. It is made available under aCC-BY 4.0 International license.

Figure 7

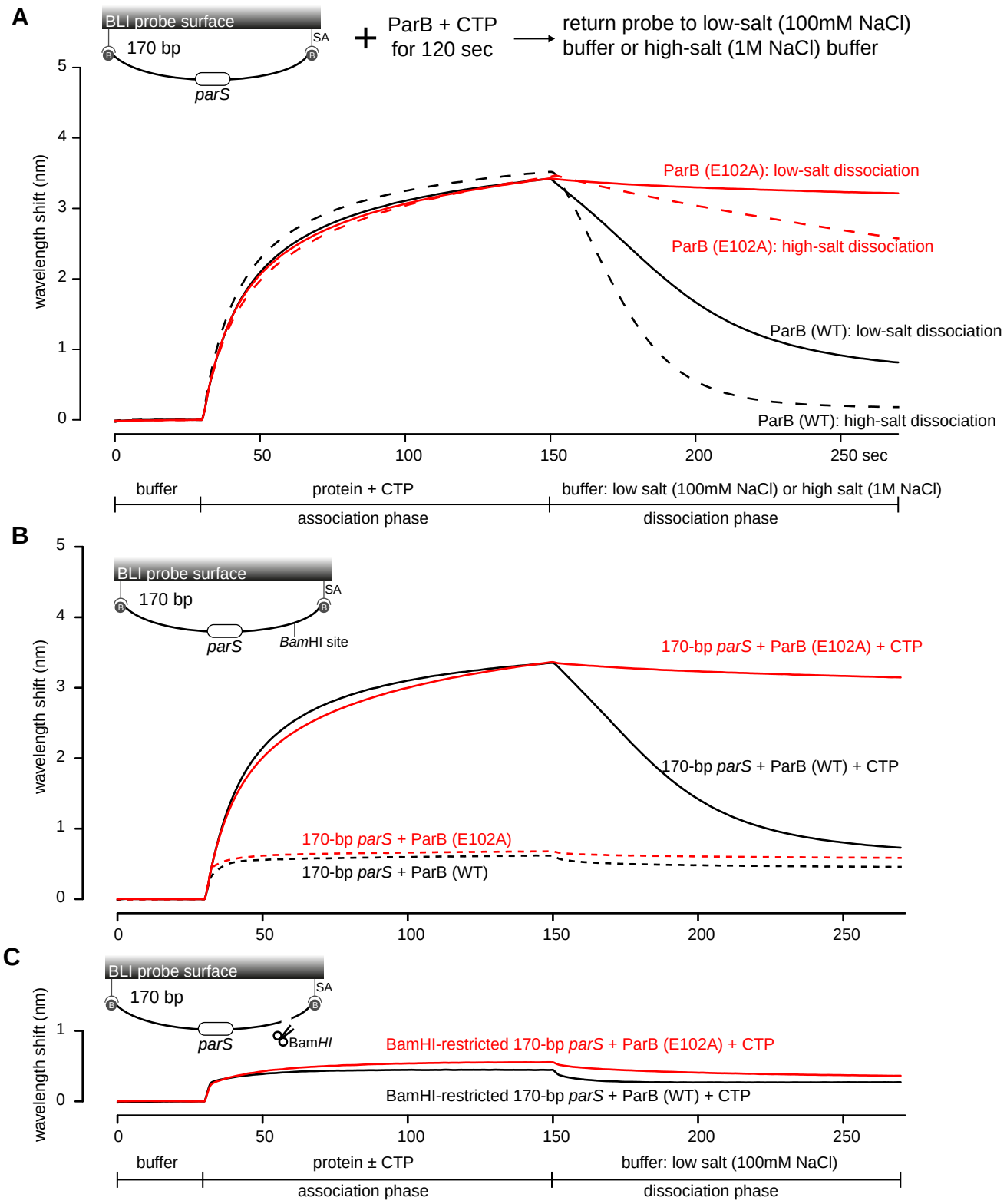

Figure 7. The DNA-entrapped ParB (E102A)-CTP clamp is resistant to high-salt conditions. (A) BLI analysis of the interaction between a premix of 1 µM *C. crescentus* ParB (WT) or ParB (E102A) + 1 mM CTP and 170-bp dual biotin-labeled *parS* DNA. For the dissociation phase, the probe was returned to a low-salt buffer that contains 100 mM NaCl (solid black or red lines) or to a high-salt buffer that contains 1 M NaCl (dashed black or red lines). The schematic diagram of the BLI probe shows a closed *parS* DNA substrate due to the interactions between a dual biotin-labeled DNA and the streptavidin (SA)-coated probe surface. **(B)** BLI analysis of the interaction between a premix of 1 µM *C. crescentus* ParB (WT) or ParB (E102A) + 1 mM CTP (solid lines) or - 1 mM CTP (dashed lines) and 170-bp dual biotin-labeled *parS* DNA. **(C)** Same as panel B but immobilized DNA fragments have been restricted with BamHI before BLI analysis.

bioRxiv preprint doi: https://doi.org/10.1101/816959; this version posted May 5, 2021. The copyright holder for this preprint (which was not certified by peer review) is the author/funder, who has granted bioRxiv a license to display the preprint in perpetuity. It is made available under aCC-BY 4.0 International license.

FIGURE 8

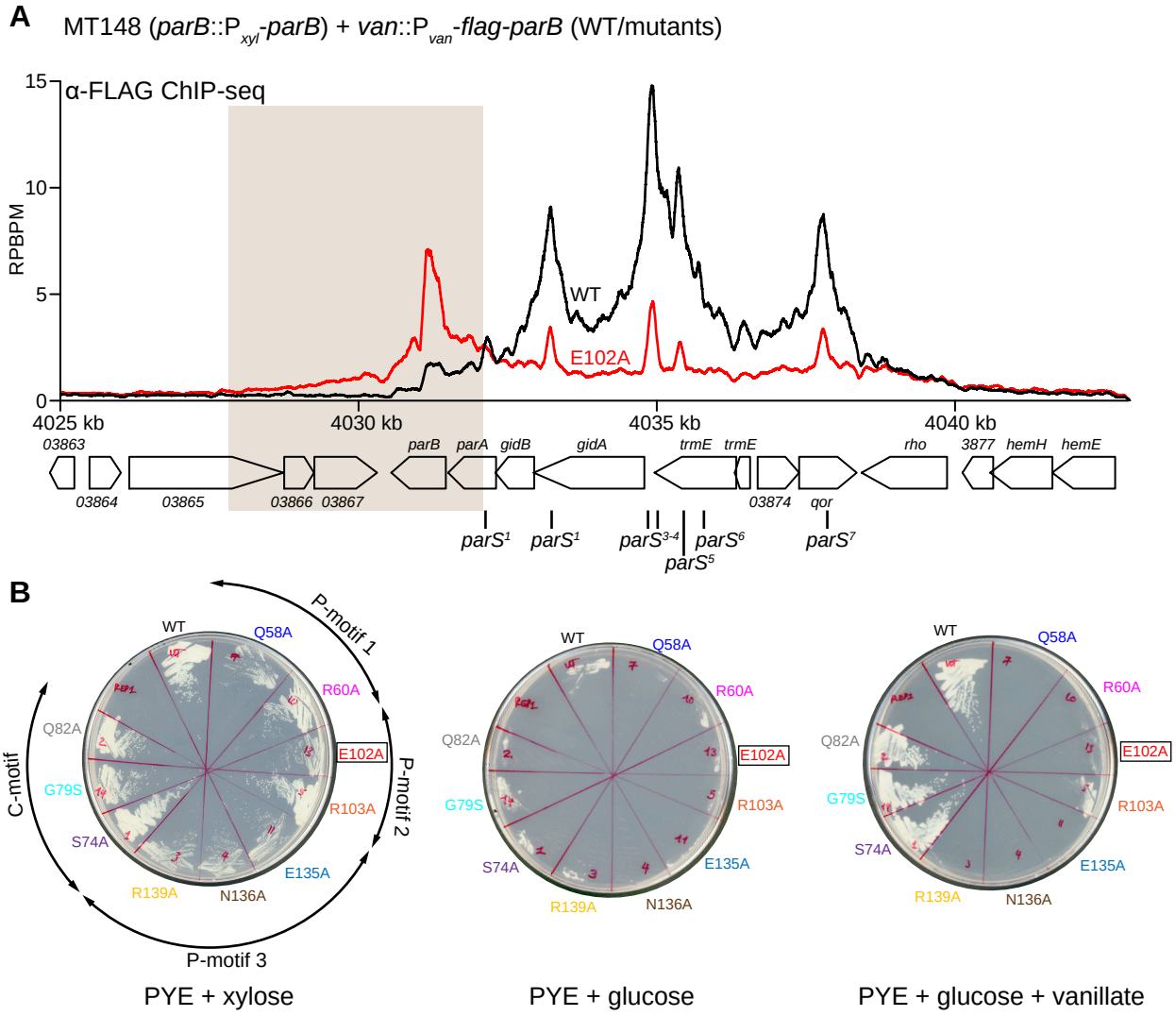

Figure 8. ParB (E102A) occupies a more extended DNA region surrounding *parS* sites than ParB (WT) *in vivo*. (A) ChIP-seq showed the distribution of FLAG-tagged ParB (WT) (black) and FLAG-ParB (E102A) (red) on *C. crescentus* chromosome between +4025 kb and +4042 kb. Underlying genes and *parS* sites are also shown below ChIP-seq profiles. ChIP-seq signals were reported as the number of reads per base pair per million mapped reads (RPBPM). **(B)** The FLAG-tagged version of ParB (WT) is functional and could complement the depletion of wild-type untagged ParB while the "clamp-locked" mutant ParB (E102A) could not. *C. crescentus* strains *parB::*P_{xyl}*-parB van::*P_{van}*-flag-parB* (WT or mutants) were restruck on PYE + xylose to induce the expression of the native ParB, or on PYE + glucose to repress the expression of the native ParB, or on PYE + glucose + vanillate to repress the expression of the native ParB while expressing the FLAG-tagged ParB (WT/mutants).

bioRxiv preprint doi: https://doi.org/10.1101/816959; this version posted May 5, 2021. The copyright holder for this preprint (which was not certified by peer review) is the author/funder, who has granted bioRxiv a license to display the preprint in perpetuity. It is made available under aCC-BY 4.0 International license.

FIGURE 9

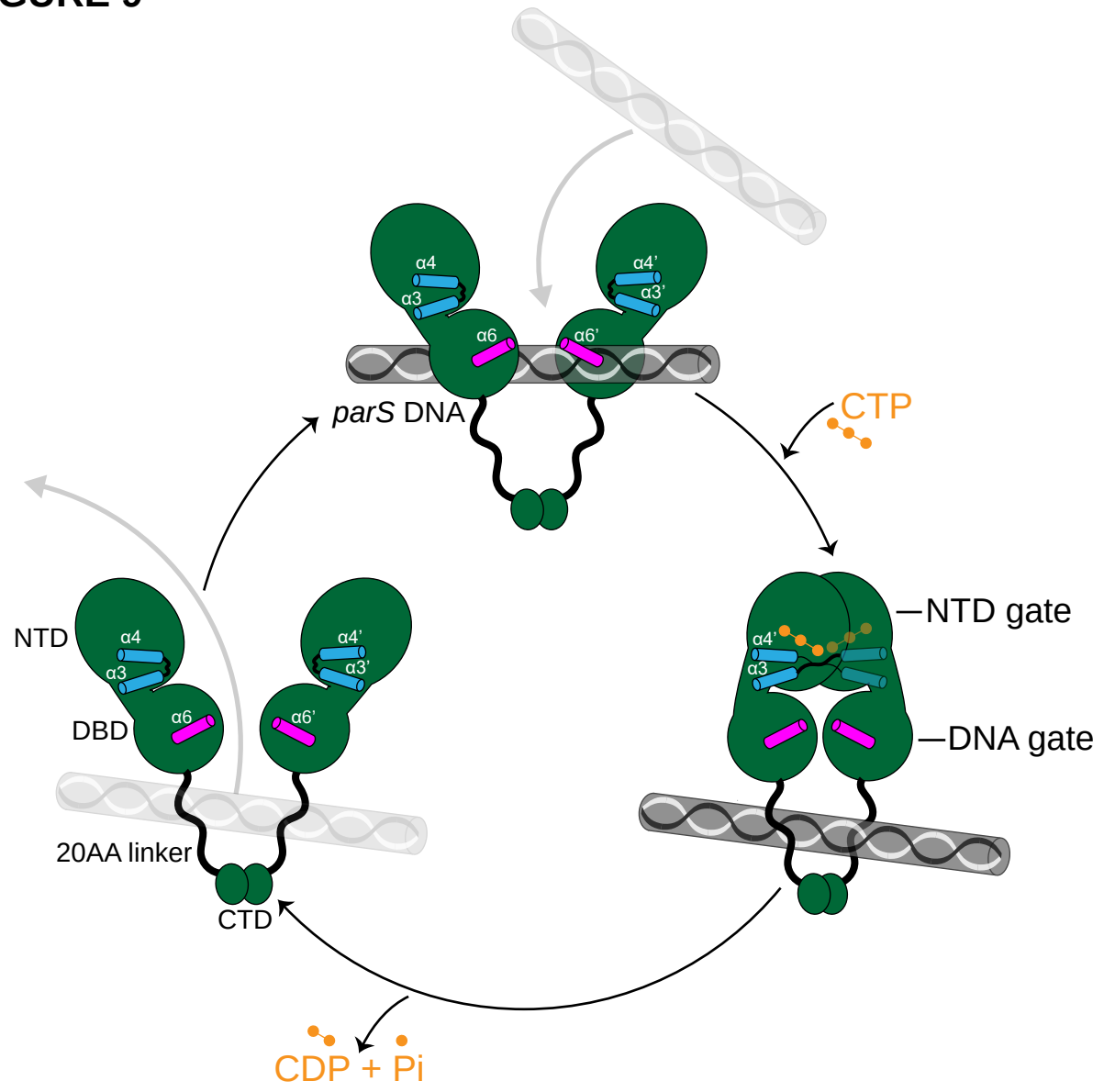

Figure 9. A model for *C. crescentus* ParB nucleating and sliding cycle. ParB (dark green) consists of three domains: an N-terminal CTP-binding domain (NTD), a central *parS* DNA-binding domain (DBD), a C-terminal dimerization domain (CTD), and a 20 amino acid linker that connects the DBD and the CTD together. Nucleating ParB is an open clamp, in which *parS* DNA is captured at the DNA-binding domain (the DNA-gate). Upon binding CTP (orange), the N-terminal domain (NTD) self-dimerizes to close the NTD-gate of the clamp. CTP-binding and the exchange of helices α4 and α4' (blue) stabilize this closed conformation. The DNA-binding domains also move closer together to close the DNA-gate, potentially driving *parS* DNA into a compartment between the DNA-gate and the C-terminal domain. In the nucleotide-bound state, the DBD and the DNA-recognition helices (α6 and α6', magenta) are incompatible with DNA binding. CTP hydrolysis and/or the release of hydrolytic products (CDP and inorganic phosphate Pi) may re-open the gates to discharge DNA.

bioRxiv preprint doi: https://doi.org/10.1101/816959; this version posted May 5, 2021. The copyright holder for this preprint (which was not certified by peer review) is the author/funder, who has granted bioRxiv a license to display the preprint in perpetuity. It is made available under aCC-BY 4.0 International license.

Figure 1-figure supplement 1

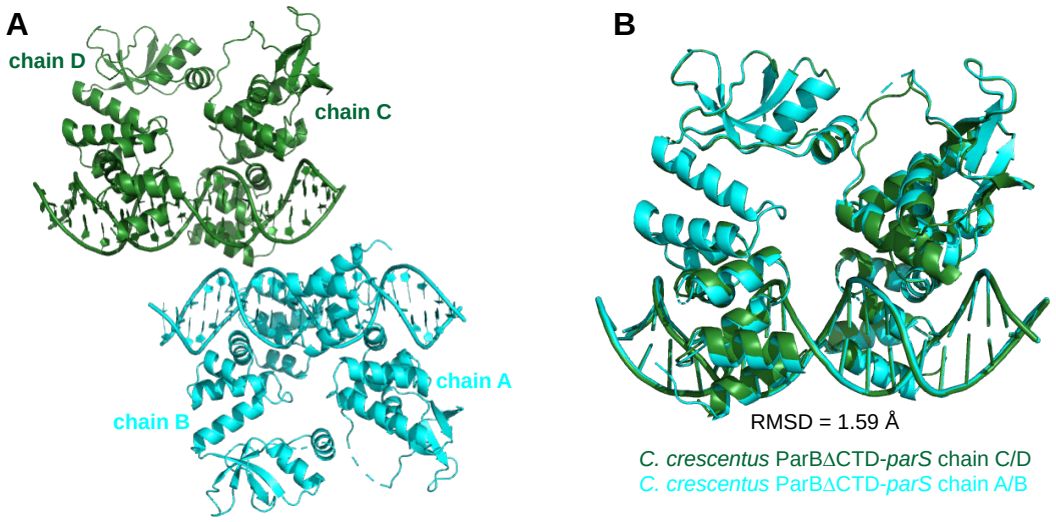

Figure1-figure supplement 1. The composition of the asymmetric unit (ASU) of the *C. crescentus* ParBΔCTD-*parS* co-crystal. (A) The ASU contains four copies of the *C. crescentus* ParBΔCTD monomers (chain A, B, C, and D) and two copies of the full-size *parS* DNA. **(B)** Superimposition of the chain C-D-*parS* complex (dark green) to the chain A-B-*parS* complex (cyan) shows that the two complexes in the ASU are structurally similar (RMSD = 1.59 Å).

bioRxiv preprint doi: https://doi.org/10.1101/816959; this version posted May 5, 2021. The copyright holder for this preprint (which was not certified by peer review) is the author/funder, who has granted bioRxiv a license to display the preprint in perpetuity. It is made available under aCC-BY 4.0 International license.

Figure 1-figure supplement 2

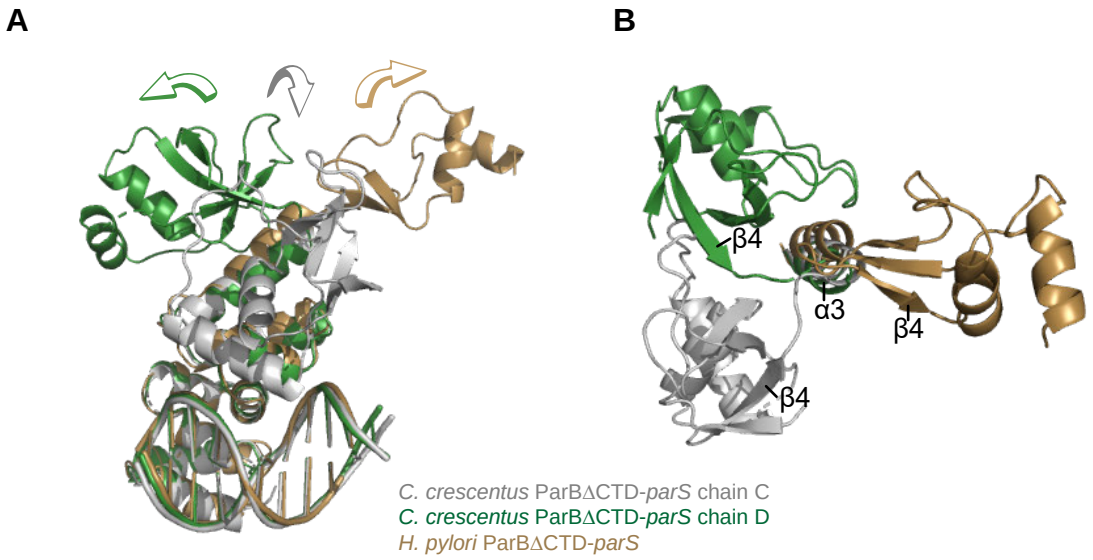

Figure 1-figure supplement 2. Structural comparisons of the *C. crescentus* ParBΔCTD-*parS* complex to the *H. pylori* ParBΔCTD-*parS* complex. (A) A side-view of the superimposition between *C. crescentus* ParBΔCTD chain C (grey), chain D (dark green), and *H. pylori* ParBΔCTD (golden) shows the three distinct orientations of the NTD. **(B)** A top view of the superimposition between *C. crescentus* ParBΔCTD chain C, chain D, and *H. pylori* ParBΔCTD. The *parS* DNA, DBD, and helix α4 are omitted for clarity.

bioRxiv preprint doi: https://doi.org/10.1101/816959; this version posted May 5, 2021. The copyright holder for this preprint (which was not certified by peer review) is the author/funder, who has granted bioRxiv a license to display the preprint in perpetuity. It is made available under aCC-BY 4.0 International license.

Figure 2-figure supplement 1

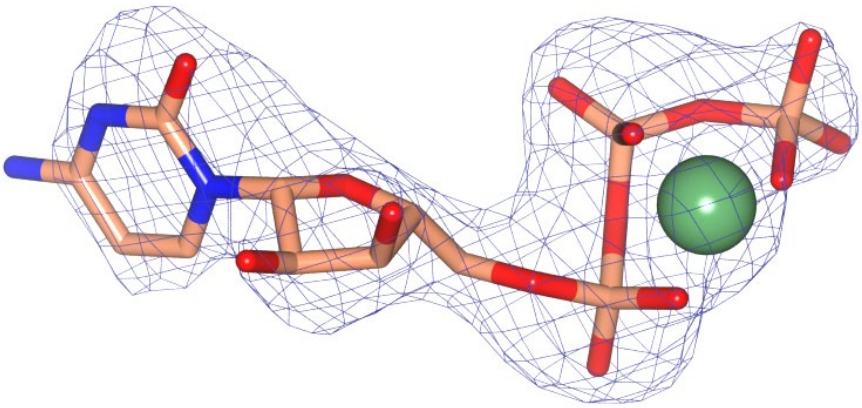

Figure 2-figure supplement 1. Omit mFobs-DFcalc difference electron density calculated at 2.73 Å resolution for Mg-CTP. The omit map was calculated using phases from the final model, with the displayed atoms omitted, after the application of small random shifts to the atomic coordinates, re-setting temperature factors, and re-refining to convergence (rendered in blue mesh at a contour level of ~3.5σ).

bioRxiv preprint doi: https://doi.org/10.1101/816959; this version posted May 5, 2021. The copyright holder for this preprint (which was not certified by peer review) is the author/funder, who has granted bioRxiv a license to display the preprint in perpetuity. It is made available under aCC-BY 4.0 International license.

Figure 2-figure supplement 2

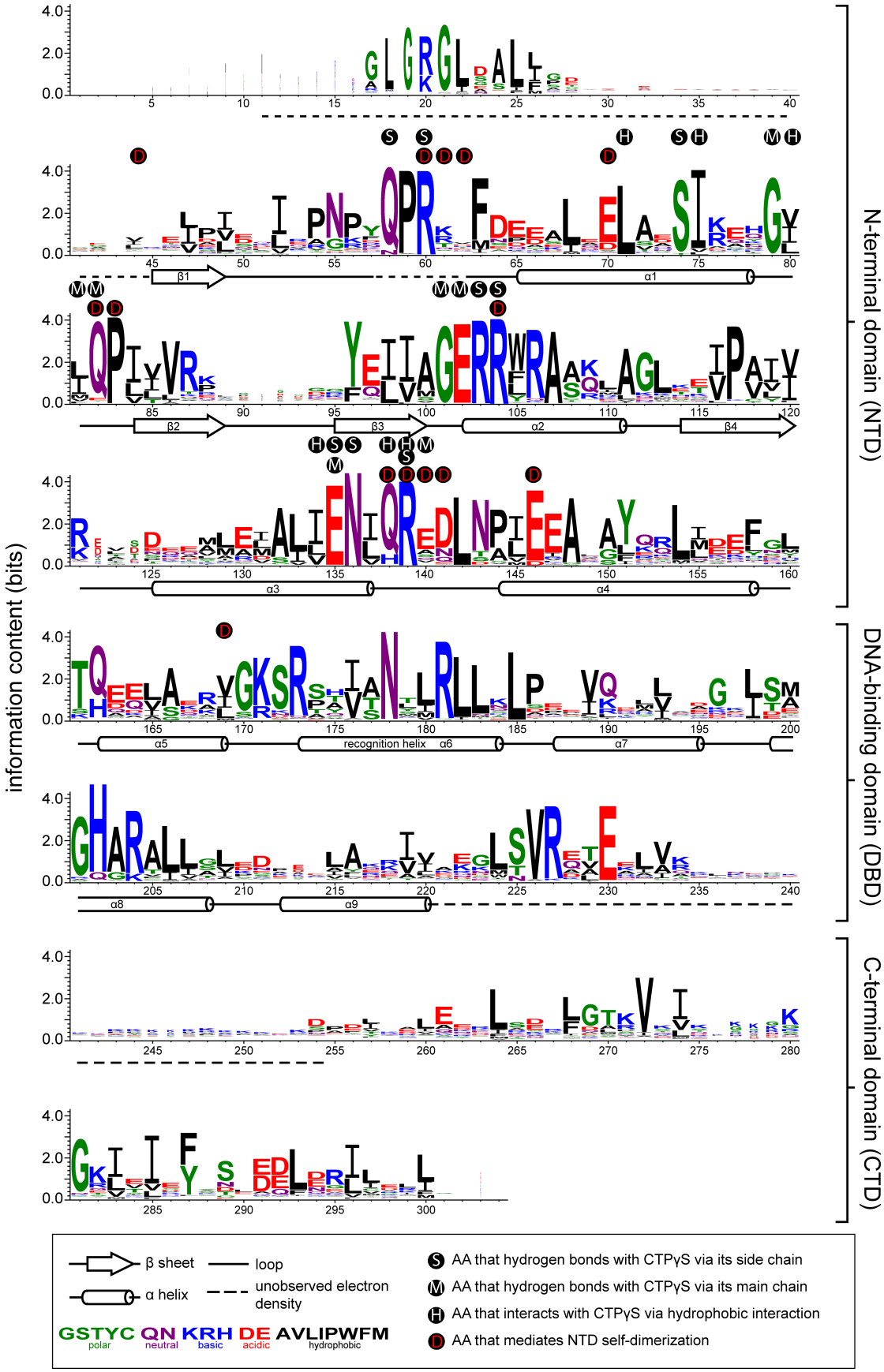

Figure 2-figure supplement 2. Sequence alignment of the chromosomal ParB protein family. An alignment of ~1800 chromosomal ParB proteins was constructed and presented as a sequence logo. The height of the stack indicates the sequence conservation, while the height of symbols within the stack indicates the relative frequency of each amino acid residue at that position. Amino acids are colored based on their chemical properties. Secondary-structure elements for *C. crescentus* ParBΔCTD are shown below the alignment. Dashed lines indicate unmodelled residues due to poor electron density in the *C. crescentus* ParBΔCTD-CTPɣS co-crystal structure. Residues that contact CTPɣS-Mg^{2+} and/or mediate the NTD self-dimerization are also labeled.

bioRxiv preprint doi: https://doi.org/10.1101/816959; this version posted May 5, 2021. The copyright holder for this preprint (which was not certified by peer review) is the author/funder, who has granted bioRxiv a license to display the preprint in perpetuity. It is made available under aCC-BY 4.0 International license.

Figure 2-figure supplement 3

A

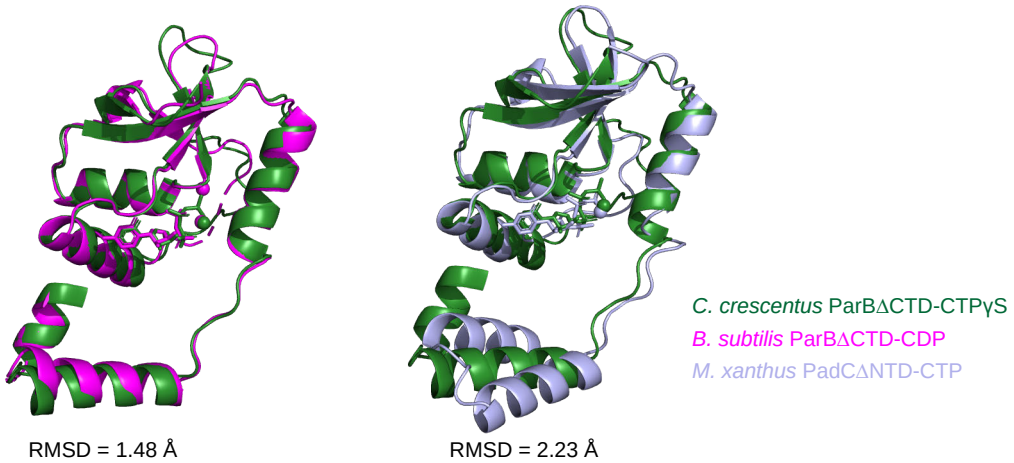

B

	C. crescentus ParBΔCTD-CTPγS	*Bacillus subtilis* ParBΔCTD-CDP (6SDK, Soh *et al*., 2019)	*Myxococcus xanthus* PadCΔNTD-CTP (6RYK, Osorio-Valeriano *et al*., 2019)
P-motif 1	Q58 (side chain) R60 (side chain)	Q37 (no contact to CDP) R39 (side chain)	F308 (no contact to CTP) R311 (side chain)
C-motif	S74 (side chain) G79 (main chain) L81 (main chain) Q82 (main chain)	S53 (side chain) G58 (main chain) L60 (main chain) Q61 (main chain)	E322 (side chain) G327 (main chain) L329 (main chain) F330 (main chain)
P-motif 2	G101 (main chain) E102 (main chain) R103 (side chain) R104 (side chain)	G77 (main chain, via Ca^{2+}) E78 (main chain, via Ca^{2+}) R79 (side chain) R80 (side chain)	G347 (main chain) F348 (main chain) R349 (side chain) R350 (side chain)
P-motif 3	E135 (side chain, via Mg^{2+}) E135 (main chain, opposite subuit) N136 (side chain, via Mg^{2+}) R139 (side chain) A140 (main chain, opposite subunit)	E111 (side chain, via H_20 and Ca^{2+}) E111 (main chain, opposite subunit) N112 (side chain, via H_20 and Ca^{2+}) R115 (side chain) E116 (main chain, opposite subunit)	E382 (side chain, via H_20 and Mg^{2+}) E382 (main chain, opposite subunit) A383 (no contact to CTP) A386 (no contact to CTP) T387 (main chain, opposite subunit)
Hydrophobic interactions	L71 (side chain)	L50 (side chain)	L319 (side chain)
to the cytidine moiety	I134 (side chain) I75 (side chain) V80 (side chain)	I110 (side chain) V54 (side chain) I59 (side chain)	A381 (no contact with CTP) I323 (side chain) Q328 (side chain)
to the ribose moiety	R139 (side chain)	R115 (side chain)	A386 (no contact to CTP)
to the cytidine and ribose moiety	Q138 (side chain)	Q114 (side chain)	H385 (side chain)

Figure 2-figure supplement 3. Structural comparisons of the *C. crescentus* ParBΔCTD-CTPγS complex to the *B. subtilis* ParBΔCTD-CDP complex and the *M. xanthus* PadCΔNTD-CTP complex. (A) Superimposition of nucleotide-bound structures of *C. crescentus* ParBΔCTD (dark green), *B. subtilis* ParBΔCTD (magenta), and *M. xanthus* PadCΔNTD (light blue) with their corresponding pairwise root-mean-square deviation values (RMSD). **(B)** Summary of nucleotide-contacting residues from *C. crescentus* ParBΔCTD-CTPγS structure, *B. subtilis* ParBΔCTD-CDP structure (PDB accession code: 6SDK), and *M. xanthus* PadCΔNTD structure (PDB accession code: 6RYK). Positional equivalent residues that do not contact nucleotides are shown in light grey.

bioRxiv preprint doi: https://doi.org/10.1101/816959; this version posted May 5, 2021. The copyright holder for this preprint (which was not certified by peer review) is the author/funder, who has granted bioRxiv a license to display the preprint in perpetuity. It is made available under aCC-BY 4.0 International license.

Figure 4-figure supplement 1

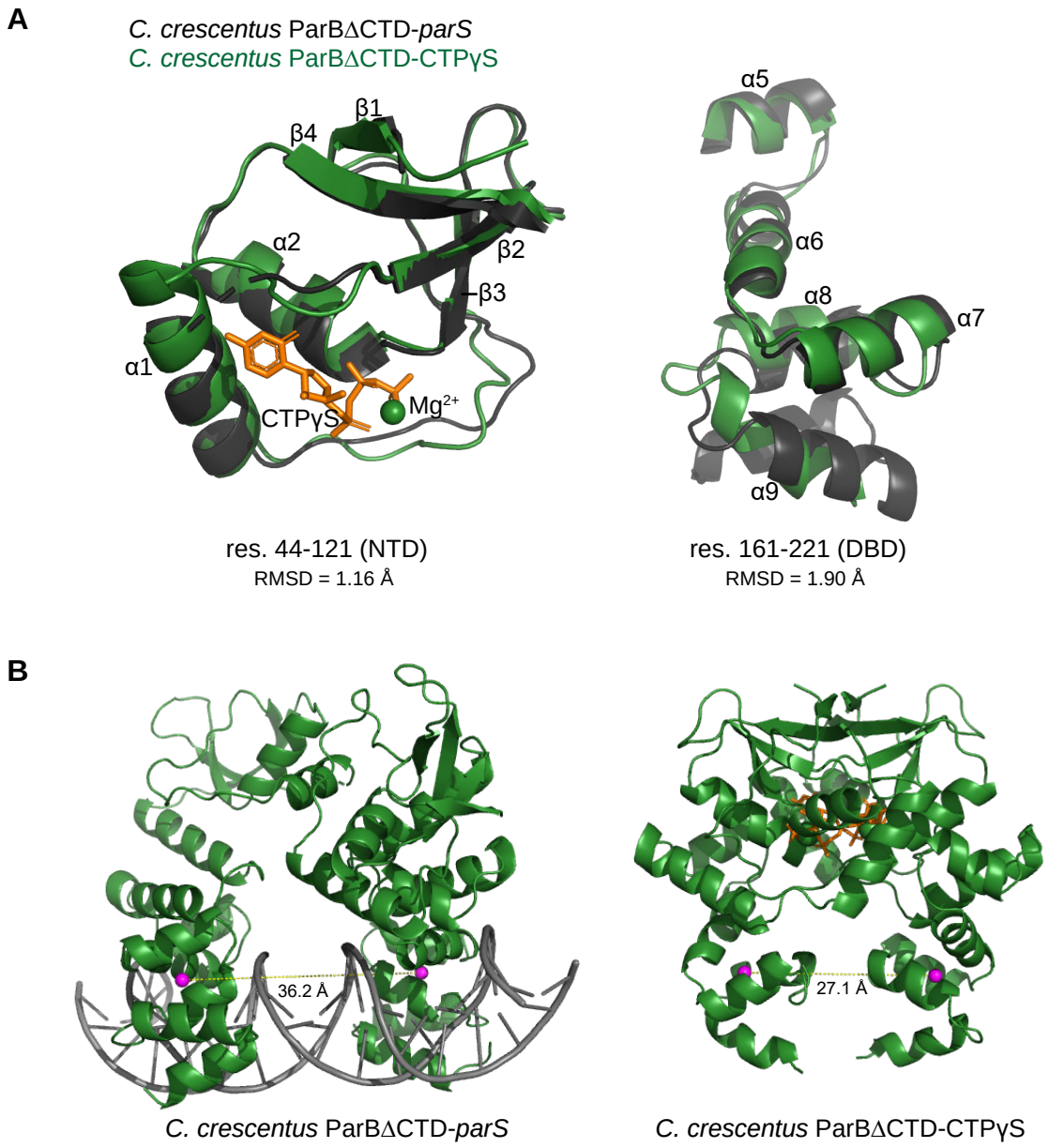

Figure 4-figure supplement 1. The structure of nucleotide-bound *C. crescentus* ParBΔCTD is incompatible with specific *parS* binding at the DBD. (A) Residues 44 to 121 of the NTD and residues 161 to 221 of the DBD move in a near rigid-body motion between the ParBΔCTD-*parS* and the ParBΔCTD-CTPγS structures. **(Left panel)** Structural comparison between the NTDs (residues 44 to 121) from the ParBΔCTD-*parS* structure (black) and the ParBΔCTD-CTPγS structure (dark green). **(Right panel)** Structural comparison between the DBDs (residues 161 to 221) from the ParBΔCTD-*parS* structure (black) and the ParBΔCTD-CTPγS structure (dark green). The corresponding root-mean-square deviation value (RMSD) is shown below each structural alignment. **(B)** The inter-domain distances between opposite DBDs in the ParBΔCTD-*parS* and the ParBΔCTD-CTPγS structures. Distances (yellow dashed lines) were measured between the centroid (magenta sphere) of each DBD.

bioRxiv preprint doi: https://doi.org/10.1101/816959; this version posted May 5, 2021. The copyright holder for this preprint (which was not certified by peer review) is the author/funder, who has granted bioRxiv a license to display the preprint in perpetuity. It is made available under aCC-BY 4.0 International license.

Figure 5-figure supplement 1

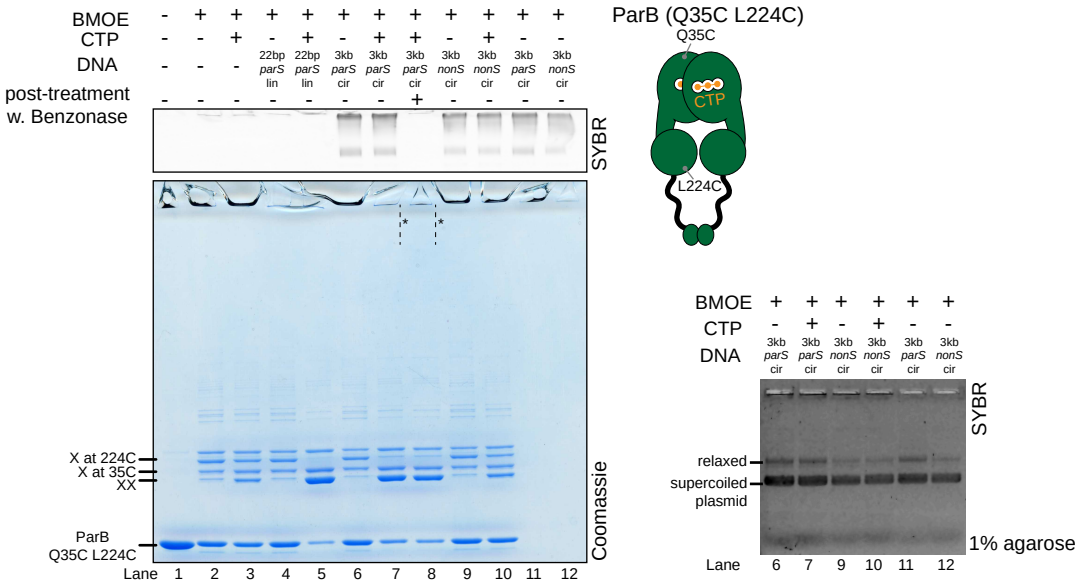

Figure 5-figure supplement 1. Crosslinking ParB (Q35C L224C) did not produce a HMW smear despite the presence of CTP and a circular *parS* plasmid. (Left panel) Denaturing polyacrylamide gel analysis of BMOE crosslinking products of 8 µM dual-cysteine ParB (Q35C L224C) variant ± 0.5 µM DNA ± 1 mM CTP. Different DNA were employed in crosslinking reactions: a linear 22-bp *parS* DNA (22 bp *parS* lin), a circular 3-kb *parS* plasmid (3 kb *parS* cir), and a circular 3-kb scrambled *parS* plasmid (3 kb *nonS* cir). The high molecular weight (HMW) smear near the top of the polyacrylamide gel was not observed, with or without a Benzonase post-treatment (dashed lines and asterisks, Lanes 7 and 8). The polyacrylamide gel was also stained with a DNA-dye, Sybr Green (SYBR), and only the top section of the gel was shown. Small 22-bp *parS* DNA duplex migrated out of the gel, thus was not observed near the top of the Sybr-stained gel. A schematic diagram of a dual-cysteine *C. crescentus* ParB dimer is also shown. **(Right panel)** Agarose gel analysis of BMOE crosslinking products. A subset of crosslinking reactions (Lanes 6, 7, and 9-12) were loaded and resolved on 1% agarose gel. The gel was subsequently stained with Sybr Green for DNA. Shifted gel bands were marked with a solid line and an asterisk.

bioRxiv preprint doi: https://doi.org/10.1101/816959; this version posted May 5, 2021. The copyright holder for this preprint (which was not certified by peer review) is the author/funder, who has granted bioRxiv a license to display the preprint in perpetuity. It is made available under aCC-BY 4.0 International license.

Figure 5-figure supplement 2

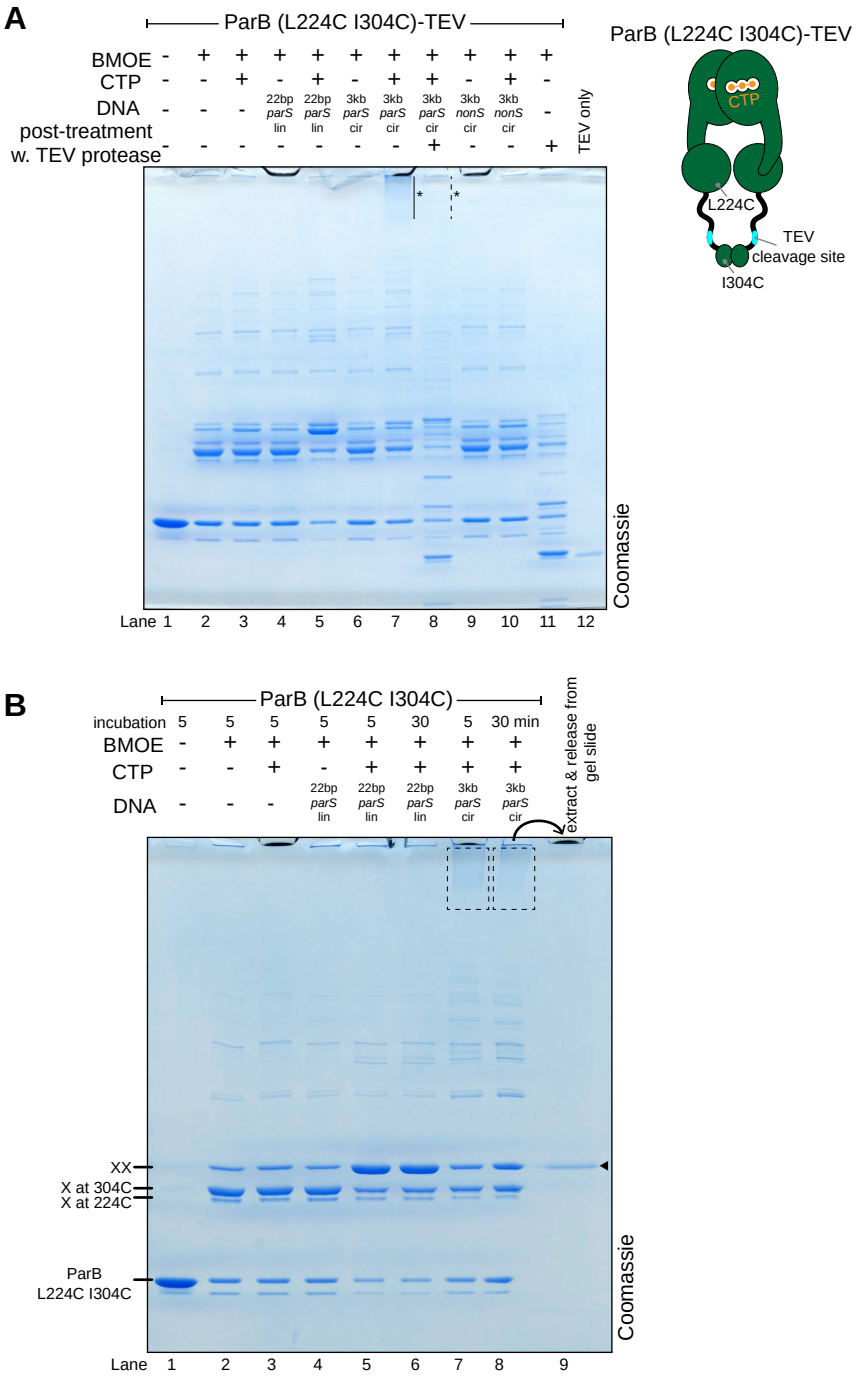

Figure 5-figure supplement 2. The high molecular weight (HMW) smear likely contains catenates between crosslinked ParB dimers and circular *parS* plasmids. (A) A post-crosslinking treatment of a ParB (L224C I304C)TEV variant with TEV protease eliminated the HMW smear. A dual-cysteine ParB variant was engineered with a TEV protease cleavage site in the DBD-CTD linker (see the schematic diagram). This ParB (L224C I304C)TEV variant was purified and used in a BMOE crosslinking reactions in the presence or absence of 1 mM CTP and 0.5 µM DNA. Different DNA were employed in crosslinking reactions: a linear 22-bp *parS* DNA (22 bp *parS* lin), a circular 3-kb *parS* plasmid (3 kb *parS* cir), and a circular 3-kb scrambled *parS* plasmid (3 kb *nonS* cir). In contrast to Lane 7, the HMW smear near the top of the polyacrylamide gel was no longer observed when TEV was added after the crosslinking reactions was quenched (Lane 8, dashed line and asterisk). **(B)** Double-crosslinked ParB (L224C I304C) dimer is the major protein species in the HMW smear. Gel slides encompassing the HMW smear was crushed and soaked in a Benzonase-supplemented buffer to release bound proteins. The released protein was analyzed on a denaturing polyacrylamide gel (Lane 9). The solid arrow indicates the position of a double-crosslinked ParB (L224C I304C).

bioRxiv preprint doi: https://doi.org/10.1101/816959; this version posted May 5, 2021. The copyright holder for this preprint (which was not certified by peer review) is the author/funder, who has granted bioRxiv a license to display the preprint in perpetuity. It is made available under aCC-BY 4.0 International license.

Figure 6-figure supplement 1

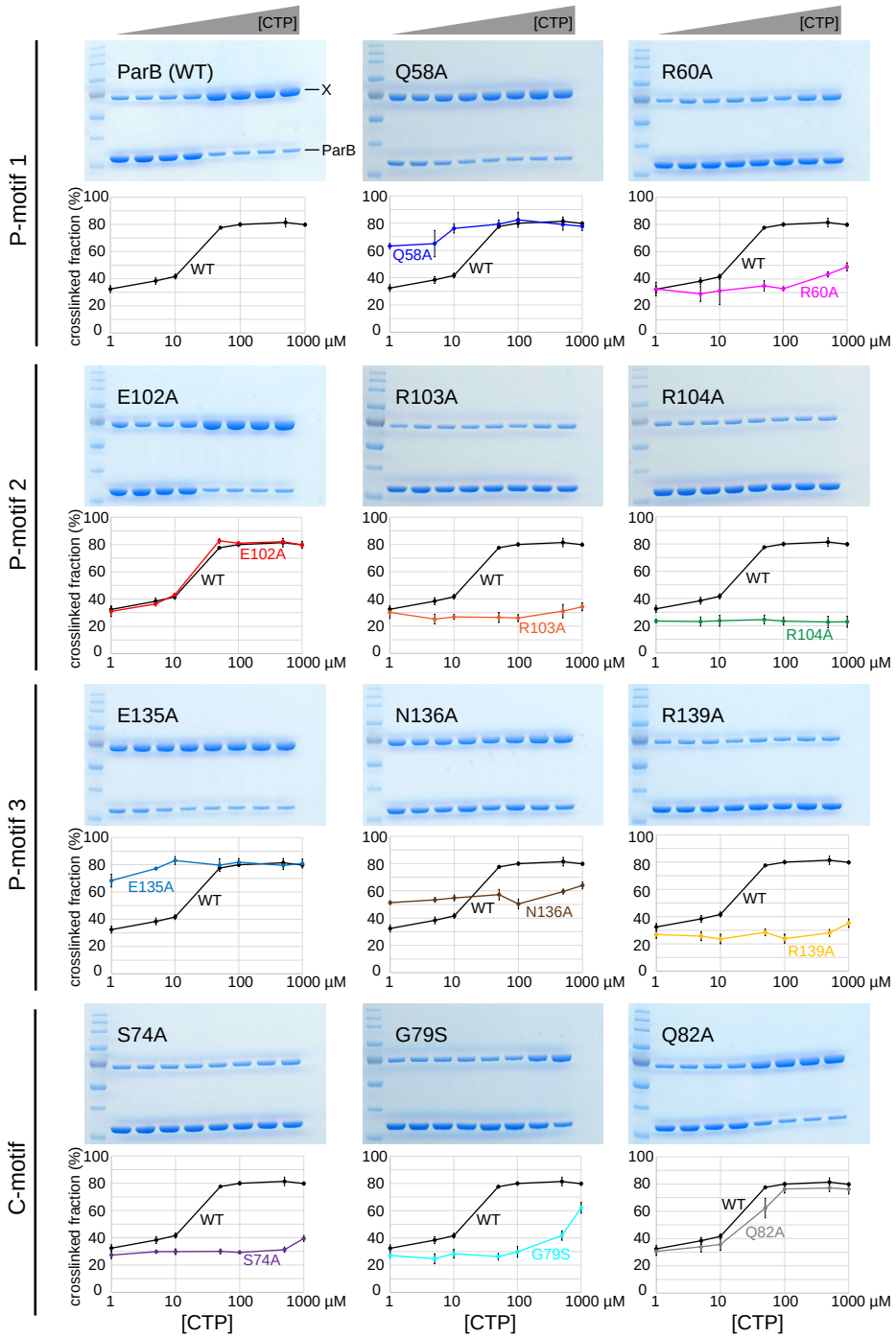

Figure 6-figure supplement 1. Denaturing polyacrylamide gel analysis of crosslinking products of alanine scanning ParB variants. Purified ParB variants (8 μM) were preincubated with 0.5 μM 22-bp *parS* DNA, and an increasing concentration of CTP for 5 minutes before BMOE was added. Crosslinking products were resolved on a 12% denaturing polyacrylamide gel and the crosslinked fractions (X) were quantified. Error bars represent SD from three replicates.

bioRxiv preprint doi: https://doi.org/10.1101/816959; this version posted May 5, 2021. The copyright holder for this preprint (which was not certified by peer review) is the author/funder, who has granted bioRxiv a license to display the preprint in perpetuity. It is made available under aCC-BY 4.0 International license.

Figure 6-figure supplement 2

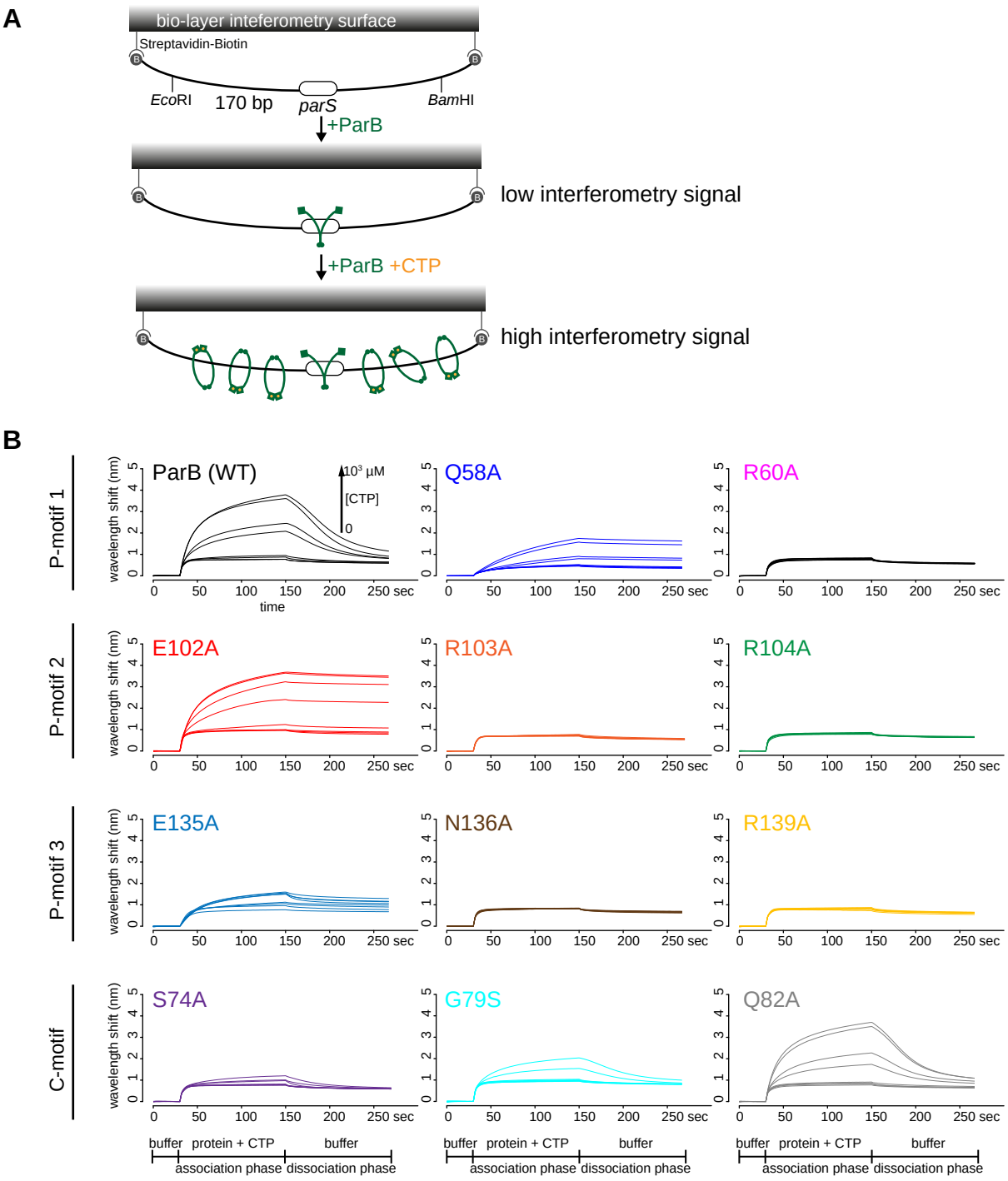

Figure 6-figure supplement 2. Bio-layer interferometry (BLI) analysis of the interaction between ParB variants and a 170-bp closed *parS* DNA substrate. (A) A schematic diagram of the BLI assay. A dual biotin-labeled 170-bp *parS* DNA was tethered to the streptavidin (SA)-coated probe to create a DNA substrate where both ends were blocked (a closed DNA substrate). BLI assay monitors wavelength shifts (nm) resulting from changes in the optical thickness of the sensor surface during association or dissociation of the analyte. In the absence of CTP, ParB (WT) (green) nucleates at *parS* only. In the presence of CTP (orange), ParB (WT) slides on and entraps DNA to accumulate on the closed DNA substrate, thus giving rise to an elevated BLI response. **(B)** Representative BLI sensorgrams of the interactions between ParB variants and the closed DNA substrate in the presence of an increasing concentration of CTP. The BLI probe with tethered *parS* DNA substrate was dipped into a buffer only solution (0-30 s), then to a premix of 1 μM ParB ± an increasing concentration of CTP (30-150 s: association phase), and finally returned to a buffer-only solution (150-270 s: dissociation phase).

bioRxiv preprint doi: https://doi.org/10.1101/816959; this version posted May 5, 2021. The copyright holder for this preprint (which was not certified by peer review) is the author/funder, who has granted bioRxiv a license to display the preprint in perpetuity. It is made available under aCC-BY 4.0 International license.

Figure 8-figure supplement 1

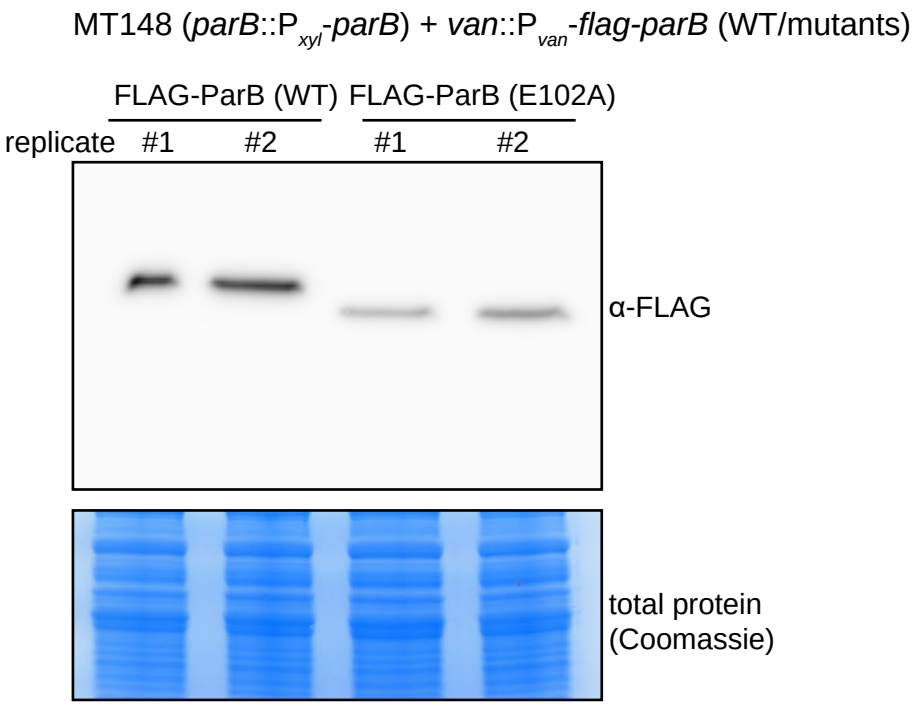

Figure 8-figure supplement 1. Immunoblot analysis of FLAG-tagged ParB (WT) vs. E102A. Cells were depleted of wild-type untagged ParB for four hours, then vanillate was added for an additional hour to allow for expression of FLAG-tagged ParB (WT/E102A). Equal amount of total protein was loaded in each well of the SDS-PAGE. Biological replicates are shown.

bioRxiv preprint doi: https://doi.org/10.1101/816959; this version posted May 5, 2021. The copyright holder for this preprint (which was not certified by peer review) is the author/funder, who has granted bioRxiv a license to display the preprint in perpetuity. It is made available under aCC-BY 4.0 International license.

SUPPLEMENTARY FILE 1. PLASMIDS, OLIGOS, AND PROTEIN SEQUENCES

Plasmids/DNA	Description	Source
pET21b::*C. crescentus* ParB-His_6	Overexpression of a C-terminally His_6-tagged *C. crescentus* ParB, carbenicillin^R >*C. crescentus* ParB (WT)-His_6 MSEGRRGLGRGLSALLGEVDAAPA**Q**^{35}APGEQLGGSREAP IEILQRNPDQPRRTFREEDLEDLSNSIREKGVLQPILVRPSP DTAGEYQIVAGER**R**^{104}WRAAQRAGLKTVPIMVRELDDLAVL EIGIIENVQRADLNVLEEALSYKVLMEKFERTQENIAQTIGKS RSHVANTMRLLALPDEVQSYLVSGELTAGHARAIAAAADPV ALAKQIIEGGLSVRETEALARKAPNLSAGKSKGGRPPRVKD TDTQALESDLSSVLGLDVSIDHRGSTGTLTITYATLEQLDDL **C**^{297}NRLTRGIKLAAALEHHHHHH* (numbering according to [1])	Gift from C. Jacob-Wagner [2]
pET21b::*C. crescentus* ParBΔCTD-His_6	Overexpression of a C-terminally truncated His_6-tagged *C. crescentus* ParB (the last 50 amino acids of ParB were removed), carbenicillin^R	This study
pET21b::*C. crescentus* ParB (Q58A)-His_6	Overexpression of a C-terminally His_6-tagged *C. crescentus* ParB (Q58A), carbenicillin^R	This study
pET21b::*C. crescentus* ParB (R60A)-His_6	Overexpression of a C-terminally His_6-tagged *C. crescentus* ParB (R60A), carbenicillin^R	This study
pET21b::*C. crescentus* ParB (E102A)-His_6	Overexpression of a C-terminally His_6-tagged *C. crescentus* ParB (E102A), carbenicillin^R	This study
pET21b::*C. crescentus* ParB (R103A)-His_6	Overexpression of a C-terminally His_6-tagged *C. crescentus* ParB (R103), carbenicillin^R	This study
pET21b::*C. crescentus* ParB (R104A)-His_6	Overexpression of a C-terminally His_6-tagged *C. crescentus* ParB (R104A), carbenicillin^R	This study
pET21b::*C. crescentus* ParB (E135A)-His_6	Overexpression of a C-terminally His_6-tagged *C. crescentus* ParB (E135A), carbenicillin^R	This study
pET21b::*C. crescentus* ParB (N136A)-His_6	Overexpression of a C-terminally His_6-tagged *C. crescentus* ParB (N136A), carbenicillin^R	This study
pET21b::*C. crescentus* ParB (R139A)-His_6	Overexpression of a C-terminally His_6-tagged *C. crescentus* ParB (R139A), carbenicillin^R	This study
pET21b::*C. crescentus* ParB (S74A)-His_6	Overexpression of a C-terminally His_6-tagged *C. crescentus* ParB (S74A), carbenicillin^R	This study
pET21b::*C. crescentus* ParB (G79S)-His_6	Overexpression of a C-terminally His_6-tagged *C. crescentus* ParB (G79S), carbenicillin^R	This study
pET21b::*C. crescentus* ParB (Q82A)-His_6	Overexpression of a C-terminally His_6-tagged *C. crescentus* ParB (Q82A), carbenicillin^R	This study
pET21b::*C. crescentus* ParB (Q35C C297S)-His_6	Overexpression of a C-terminally His_6-tagged *C. crescentus* ParB (Q35C C297S), carbenicillin^R	[3]
pET21b::*C. crescentus* ParB (L224C C297S)-His_6	Overexpression of a C-terminally His_6-tagged *C. crescentus* ParB (Q35C C297S), carbenicillin^R	This study
pET21b::*C. crescentus* ParB (I304C C297S)-His_6	Overexpression of a C-terminally His_6-tagged *Caulobacter* ParB (Q35C C297S), carbenicillin^R	This study
pET21b::*C. crescentus* ParB (Q58A Q35C C297S)-His_6	Overexpression of a C-terminally His_6-tagged *C. crescentus* ParB (Q58A Q35C C297S), carbenicillin^R	This study
pET21b::*C. crescentus* ParB (R60A Q35C C297S)-His_6	Overexpression of a C-terminally His_6-tagged *C. crescentus* ParB (R60A Q35C C297S), carbenicillin^R	This study
pET21b::*C. crescentus* ParB (E102A Q35C C297S)-His_6	Overexpression of a C-terminally His_6-tagged *C. crescentus* ParB (E102A Q35C C297S), carbenicillin^R	This study
pET21b::*C. crescentus* ParB (R103A Q35C	Overexpression of a C-terminally His_6-tagged *C. crescentus* ParB (R103 Q35C C297S), carbenicillin^R	This study

bioRxiv preprint doi: https://doi.org/10.1101/816959; this version posted May 5, 2021. The copyright holder for this preprint (which was not certified by peer review) is the author/funder, who has granted bioRxiv a license to display the preprint in perpetuity. It is made available under aCC-BY 4.0 International license.

C297S)-His$_6$		
pET21b::*C. crescentus* ParB (R104A Q35C C297S)-His$_6$	Overexpression of a C-terminally His$_6$-tagged *C. crescentus* ParB (R104A Q35C C297S), carbenicillin^R	This study
pET21b::*C. crescentus* ParB (E135A Q35C C297S)-His$_6$	Overexpression of a C-terminally His$_6$-tagged *C. crescentus* ParB (E135A Q35C C297S), carbenicillin^R	This study
pET21b::*C. crescentus* ParB (N136A Q35C C297S)-His$_6$	Overexpression of a C-terminally His$_6$-tagged *C. crescentus* ParB (N136A Q35C C297S), carbenicillin^R	This study
pET21b::*C. crescentus* ParB (R139A Q35C C297S)-His$_6$	Overexpression of a C-terminally His$_6$-tagged *C. crescentus* ParB (R139A Q35C C297S), carbenicillin^R	This study
pET21b::*C. crescentus* ParB (S74A Q35C C297S)-His$_6$	Overexpression of a C-terminally His$_6$-tagged *C. crescentus* ParB (S74A Q35C C297S), carbenicillin^R	This study
pET21b::*C. crescentus* ParB (G79S Q35C C297S)-His$_6$	Overexpression of a C-terminally His$_6$-tagged *C. crescentus* ParB (G79S Q35C C297S), carbenicillin^R	This study
pET21b::*C. crescentus* ParB (Q82A Q35C C297S)-His$_6$	Overexpression of a C-terminally His$_6$-tagged *C. crescentus* ParB (Q82A Q35C C297S), carbenicillin^R	This study
pET21b::*C. crescentus* ParB (Q35C I304C C297S)-His$_6$	Overexpression of C-terminally His$_6$-tagged *C. crescentus* ParB (Q35C I304C C297S), carbenicillin^R	This study
pET21b::*C. crescentus* ParB (L224C I304C C297S)-His$_6$	Overexpression of C-terminally His$_6$-tagged *C. crescentus* ParB (L224C I304C C297S), carbenicillin^R	This study
pET21b::*C. crescentus* ParB (Q35C I304C C297S)-His$_6$	Overexpression of C-terminally His$_6$-tagged *C. crescentus* ParB (Q35C I304C C297S), carbenicillin^R	This study
pET21b::*C. crescentus* ParB (L224C I304C C297S)-TEV-His$_6$	Overexpression of a C-terminally His$_6$-tagged ParB (L224C I304C C297S)-TEV (a TEV cleavage site was engineered in between the C-terminal domain and the linker of ParB), carbenicillin^R >*C. crescentus* ParB (L224C I304C C297S)-TEV MSEGRRGLGRGLSALLGEVDAAPAQAPGEQLGGSREAPI EILQRNPDQPRRTFREEDLEDLSNSIREKGVLQPILVRPSP DTAGEYQIVAGERRWRAAQRAGLKTVPIMVRELDDLAVLEI GIIENVQRADLNVLEEALSYKVLMEKFERTQENIAQTIGKSR SHVANTMRLLALPDEVQSYLVSGELTAGHARAIAAAADPVA LAKQIIEGGCSVRETEALARKAPNLSAGKSKGGRPPRVKD**E** **NLYFQSGGGS**TDTQALESDLSSVLGLDVSIDHRGSTGTLTI TYATLEQLDDLSNRLTRGCKL AAALEHHHHHH* (**TEV cleavage site in bold)**	This study
pUC19::260bp-*parS*	pUC19 plasmid with 260-bp insert that contains *parS* sites, carbenicillin^R >260-bp_natural_*Caulobacter_parS*_fragment_cloned_into_pUC19 caagacgctcgcctcaatgcgaacgcccccgggttcgagcgggggcg ctggactcgatctatacgccaatcaggcgagcgggtcgatgtgactcatc ggcgtttcacgtgaaacacccccaccgcagctgtgagcggcctgtggac aatattggggatgttccacgtgaaacatcacttgccgatacagaaggtcg aaaagacccgtccaagaacgtcctcaggatcgatacggccggagatg cgctccagggcccgggc	[3]

bioRxiv preprint doi: https://doi.org/10.1101/816959; this version posted May 5, 2021. The copyright holder for this preprint (which was not certified by peer review) is the author/funder, who has granted bioRxiv a license to display the preprint in perpetuity. It is made available under aCC-BY 4.0 International license.

pUC19::260bp-scrambled *parS*	pUC19 plasmid with 260-bp insert that contains scrambled *parS* sites, carbenicillin^R >260-bp_scrambled_*Caulobacter_parS*_fragment_cloned_into_pUC19 caagacgctcgcctcaatgcgaacgcccccgggttcgagcgggggcg ctggactcgatctatacgccaatcaggcgagcgggtcgatgtgactcatc ggacagctcgagattcatcccccaccgcagctgtgagcggcctgtggac aatattggggaatcgagtatacgctactcacttgccgatacagaaggtcg aaaagacccgtccaagaacgtcctcaggatcgatacggccggagatg cgctccagggcccgggc	[3]
pUC57::attL1-*parB* (WT/mutant)-attL2	pUC57-based plasmid with phage attachment sites attL1 attL2 flanking the coding sequence of ParB (WT/mutants), Gateway-cloning compatible, kanamycin^R	Lab stock
pML477	Gateway-cloning destination vector for fusion of protein interest to an N-terminally FLAG tag, xylose-inducible promoter, medium-copy number plasmid, spectinomycin^R	Gift from M. Laub
pMT571-1xFLAG-DEST	Gateway-cloning compatible, destination vector, tetracycline^R	This study
pMT571-1xFLAG-*parB* (WT/mutants)	Expressing a FLAG-tagged version of *C. crescentus* ParB (WT/mutants), integrative at the *vanA* locus, tetracycline^R	This study
169bp_*parS*	cgccagggttttcccagtcacgacgttgtaaaacgacggccagtgaattcgagctcggtac ccgcaggaggacgtagggtagggggat**tgtttcacgtgaaaca**ggggatcctctagagtc gacctgcaggcatgcaagcttggcgtaatcatggtcatagctgtttcct (***parS* site in bold**)	[3]
FLAG-attR1-ccdB-chloramphenicol^R-attR2 cassette	gtggactacaaggacgacgacgacaagggctcggtcgaatca**acaagtttgtacaaaaaagctgaacgagaaacgtaaaatgatataaatatcaatatattaaattagattttgcataaaaaacagactacataatactgtaaaacacaacatatccagtcactatg**gcggccgcattaggcaccccaggctttacactttatgcttccggctcgtataatgtgtggattttgagttaggatccggcgagattttcaggagctaaggaagctaaaatggagaaaaaaatcactggatataccaccgttgatatatcccaatggcatcgtaaagaacattttgaggcatttcagtcagttgctcaatgtacctataaccagaccgttcagctggatattacggcctttttaaagaccgtaaagaaaaataagcacaagttttatccggcctttattcacattcttgcccgcctgatgaatgctcatccggaattccgtatggcaatgaaagacggtgagctggtgatatgggatagtgttcacccttgttacaccgttttccatgagcaaactgaaacgttttcatcgctctggagtgaataccacgacgatttccggcagtttctacacatatattcgcaagatgtggcgtgttacggtgaaaacctggcctatttccctaaagggtttattgagaatatgtttttcgtctcagccaatccctgggtgagtttcaccagttttgatttaaacgtggccaatatggacaacttcttcgcccccgttttcaccatgggcaaatattatacgcaaggcgacaaggtgctgatgccgctggcgattcaggttcatcatgccgtctgtgatggcttccatgtcggcagaatgcttaatgaattacaacagtactgcgatgagtggcagggcggggcgtaaagatctggatccggcttactaaaagccagataacagtatgcgtatttgcgcgctgatttttgcggtataagaatatatactgatatgtatacccgaagtatgtcaaaaagaggtgtgctatgaagcagcgtattacagtgacagttgacagcgacagctatcagttgctcaaggcatatatgatgtcaatatctccggtctggtaagcacaaccatgcagaatgaagcccgtcgtctgcgtgccgaacgctggaaagcggaaaatcaggaagggatggctgaggtcgcccggtttattgaaatgaacggctcttttgctgacgagaacagggactggtgaaatgcagtttaaggtttacacctataaaagagagagccgttatcgtctgtttgtggatgtacagagtgatattattgacacgcccgggcgacggatggtgatccccctggccagtgcacgtctgctgtcagataaagtctcccgtgaactttacccggtggtgcatatcggggatgaaagctggcgcatgatgaccaccgatatggccag	This study

bioRxiv preprint doi: https://doi.org/10.1101/816959; this version posted May 5, 2021. The copyright holder for this preprint (which was not certified by peer review) is the author/funder, who has granted bioRxiv a license to display the preprint in perpetuity. It is made available under aCC-BY 4.0 International license.

	tgtgccggtctccgttatcggggaagaagtggctgatctcagccaccgcgaaaatg acatcaaaaacgccattaacctgatgttctggggaatataaatgtcaggctcccttat acacagccagtctgcaggtcgac**catagtgactggatatgttgtgttttacagtat tatgtagtctgtttttttatgcaaaatctaatttaatatattgatatttatatcattttac gtttctcgttcagctttcttgtacaaagtggt (1x*flag* is underlined, attR1 and attR2 in bold)**	
Oligos	**Description**	**Source**
22-bp *parS*	ggatgtttcacgtgaaacatcc	[3]
NdeI-Ct-ParB-F	taactttaagaaggagatatacatatgtccgaagggcgtcgtggtctgggtc	This study
HindIII-Ct-ParB-R	ggtggtgctcgagtgcggccgcaagcttgtccttcacgcgtgggggcggcc	This study
P1952	ccacgatgcgaggaaacgcatatggactacaaggacgacgacgacaagggct cgg	This study
P1953	actagtggatcccccgggctgcagaccactttgtacaagaaagctgaacgagaa acg	This study

SUPPLEMENTARY FILE 2. ChIP-SEQ DATASET

ChIP-seq datasets	**GEO**
CB15N *parB*::P_{xyl}-*parB van*::P_{van}-*1xflag-parB* (WT), fixation with 1% formaldehyde, α-FLAG antibody (Sigma), ChIP fraction, replicate 1	GSE168968, this study
CB15N *parB*::P_{xyl}-*parB van*::P_{van}-*1xflag-parB* (WT), fixation with 1% formaldehyde, α-FLAG antibody (Sigma), ChIP fraction, replicate 2	GSE168968, this study
CB15N *parB*::P_{xyl}-*parB van*::P_{van}-*1xflag-parB* (E102A), fixation with 1% formaldehyde, α-FLAG antibody (Sigma), ChIP fraction, replicate 1	GSE168968, this study
CB15N *parB*::P_{xyl}-*parB van*::P_{van}-*1xflag-parB* (E102A), fixation with 1% formaldehyde, α-FLAG antibody (Sigma), ChIP fraction, replicate 2	GSE168968, this study

REFERENCES

1. Tran, N. T. *et al.* Permissive zones for the centromere-binding protein ParB on the Caulobacter crescentus chromosome. *Nucleic Acids Res* **46**, 1196–1209 (2018).
2. Lim, H. C. *et al.* Evidence for a DNA-relay mechanism in ParABS-mediated chromosome segregation. *Elife* **3**, e02758 (2014).
3. Jalal, A. S., Tran, N. T. & Le, T. B. ParB spreading on DNA requires cytidine triphosphate in vitro. *eLife* **9**, e53515 (2020).